

Structured Controller Parameter Tuning for Power Systems[☆]

Amer Mešanović^{a,b}, Ulrich Münz^d, Andrei Szabo^b, Martin Mangold^c, Joachim Bamberger^c, Michael Metzger^b, Chris Heyde^c, Rainer Krebs^c, Rolf Findeisen^a

^aLaboratory for Systems Theory and Automatic Control, Otto-von-Guericke-University Magdeburg, Germany

^bSiemens AG, Otto-Hahn-Ring 6, Munich, Germany

^cSiemens AG, Freyeslebenstr. 1, Erlangen, Germany

^dSiemens Corp., 755 College Road East, Princeton, NJ, USA

Abstract

Reliable and secure operation of power systems becomes increasingly challenging as the share of volatile generation rises, leading to largely changing dynamics. Typically, the architecture and structure of controllers in power systems, such as voltage controllers of power generators, are fixed during the design and buildup of the network. As replacing existing controllers is often undesired and challenging, setpoint adjustments, as well as tuning of the controller parameters, are possibilities to counteract changing dynamics. We present an approach for fast and computationally efficient adaptation of parameters of structured controllers based on \mathcal{H}_∞ optimization, also referred to as structured \mathcal{H}_∞ controller synthesis, tailored towards power systems. The goal of the tuning is to increase the robustness of the system towards disturbances. Conditions are established that guarantee that the approach leads to stability. The results are verified in a testbed microgrid consisting of six inverters and a load bank, as well as in several simulation studies. Furthermore, the performance of the approach is compared to other tuning approaches, thereby demonstrating significantly reduced computation times. The proposed method improves the system robustness, as well as the time-response to step disturbances and allows structured controller tuning even for large networks.

Keywords: power system control, structured controller synthesis, H-infinity design, linear matrix inequalities, distributed energy system, power oscillation damping, optimization

1. Introduction

Reliable and secure electric power supply is vital for modern life. Power systems must operate without interruptions, despite unknown disturbances, such as outages of components, unknown load dynamics, and changes in power generation. Power systems consist of prosumers, such as power plants, wind turbines and users, which are interconnected by a power grid, c.f. Fig. 1. The reliable and safe operation of power systems is “guaranteed” today by a complete automation system, consisting of, e.g., PID controllers, notch filters, and lead-lag filters, controlling power system components spanning from power plants to inverters, flexible AC transmission system elements and loads [1]. These automation systems result from careful considerations based on years of practical experience and operation. Tuning of the corresponding controller parameters is very important for reliable operation. This is currently guaranteed by tuning and verification during the installation of a component. The resulting controllers are typically not re-parameterized until a large problem in the system occurs [2]. Such manual tun-

ing has proven to be sufficient as long as the network and power plants do not change significantly. While variations in the grid are constantly present due to load fluctuations or generator outages, these variations are often predictable and can be considered during the manual tuning procedure.

Increasing amounts of renewable generation lead to large changes in the operation and the resulting dynamic behavior of the power systems [3]. Depending on the weather conditions, renewable generation can change constantly and can shift geographically. Furthermore, if the weather conditions are not suitable for renewable generation, the percentage of conventional generation needs to increase. These changes require new approaches e.g. for optimal power flow calculation or unit commitment. In this work, we focus on the effects of renewable generation on power system dynamics. The constantly shifting mix of renewable and conventional generation can lead to time-varying dynamics, i.e. oscillatory modes [4, 5, 6, 7]. If not handled, the controllers in large power systems, which are tuned today for fixed oscillatory modes, become less effective, increasing the risk of blackouts [5]. A simulation study showing the described effects can be found in [7]. Thus, new control methods are necessary to improve the robustness of power networks and to account for the changing dynamics. Furthermore, these methods will have to consider the dynamic behavior of conventional, as well as of inverter-based generation.

We propose to adapt the parameters of controllers already

[☆]This work has been partially funded by the German Federal Ministry for Economic Affairs and Energy under Grant number 03ET7541A in the frame of the DynaGridCenter project, and under Grant number 0325685A in the frame of the IREN2 project.

Email addresses: amer.mesanovic@siemens.com (Amer Mešanović), ulrich.muenz@siemens.com (Ulrich Münz), rolf.findeisen@ovgu.de (Rolf Findeisen)

present in power systems to the seemingly changing operating conditions. This approach has been recognized in the literature as a possible solution to handle time-varying dynamics [5, 6]. The overall tuning goal of the proposed approach is the reduction of the system \mathcal{H}_∞ norm, which increases the system robustness towards disturbances and typically improves the time-domain behavior. For this purpose, we introduce a controller parameter tuning method, which is applicable to a broad class of control structures and is scalable towards large scale systems, i.e. is applicable to power systems ranging from microgrids to transmission systems. We present an iterative convex optimization approach for structured \mathcal{H}_∞ controller synthesis of linear systems, which optimizes the parameters of existing controllers to current conditions in the system. We provide certificates which guarantee stability of the optimal tuned system and evaluate the effectiveness of the approach in realistic simulations, experimentally considering an inverter-only microgrid testbed.

Controller synthesis for power systems typically exploits \mathcal{H}_∞ optimization, \mathcal{H}_2 optimization, and pole placement, c.f. [8, 9, 10, 11, 12, 13, 14, 15]. Other control design and analysis approaches are sensitivity analysis [16, 17, 18], sliding mode controller design [19], the use of reference models [20], coordinated switching controllers [21], genetic algorithms based tuning [22], model predictive control [23], and time-discretization [24]. An overview of different methods for power oscillation damping can, for example, be found in [25]. However, most of the works either: consider simplified power system models [18, 12, 19]; or add and design new controllers on top of the existing power system model [23, 8, 9, 21, 13, 14, 15, 10]. These solutions require significant modification of existing control structures, which makes practical application complex and expensive. Very few publications consider the optimization of existing controller parameters [11, 26, 27]. The approaches in these works use heuristics [26], or assume a specific dependency on the parameters [11, 27].

Controller synthesis based on \mathcal{H}_∞ optimization has received significant attention in the last decades. First approaches in the 1980s used algebraic Riccati equations for the \mathcal{H}_∞ controller synthesis [28]. In the 1990s, approaches based on linear matrix inequalities became popular, leading to convex solutions for unstructured state-feedback controller synthesis based on the bounded-real lemma [29]. If the controller structure is fixed and only the parameters are tuned using \mathcal{H}_∞ optimization, as is the case in this work, one refers to structured \mathcal{H}_∞ controller design [30, 31]. Structured controller synthesis, exploiting the bounded real lemma and additional improvements and refinements are, e.g., used in [15, 32, 33, 34, 35, 36, 37, 38, 39]. Alternative tuning approaches, as non-smooth optimization [40, 41], bisection [42] etc. exist.

In recent years, the focus in structured \mathcal{H}_∞ optimization shifted towards more efficient methods to find local minima, as local solutions are often sufficient in practice. These methods are usually based on frequency sampling, leading to fast and reliable synthesis [27, 31, 43]. This, however, removes the guarantee that a stable controller will be obtained. To solve this issue, [27, 31] introduce stability constraints based on the

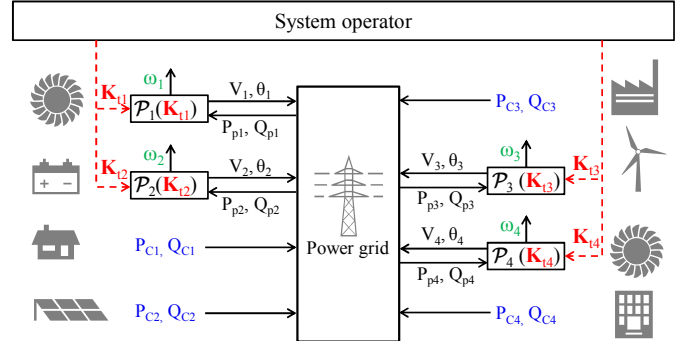


Figure 1: Exemplary power system consisting of four dynamic prosumers \mathcal{P}_i and four static prosumers $\mathcal{P}_{ci}, \mathcal{Q}_{ci}$. The tunable controller parameters \mathbf{K}_{fi} of dynamic prosumers are marked red. The static prosumers, marked with blue, are disturbance inputs into the system. The frequencies ω_i of each \mathcal{P}_i are performance outputs, marked green. For details, see Section 2.

Nyquist criterion. In [43], the assumption is made that the controlled plant is asymptotically stable, in which case the boundedness of the \mathcal{H}_∞ norm of the system sensitivity matrix is a necessary and sufficient condition for stability.

We introduce in this work a stability guarantee for structured \mathcal{H}_∞ optimization based on frequency sampling, without adding new constraints in the optimization problem. Doing so, we do not require the stability of the open loop system, as is often necessary [43]. Previous works considered structured controller synthesis with application to power systems [44, 39, 45] based on the application of the bounded real lemma. The main contributions of this work are:

- A structured \mathcal{H}_∞ controller tuning method which allows nonlinear parameter dependencies and which is scalable towards large scale systems.
- A stability certificate for the developed method.
- Two numerical studies on power transmission systems with 190 and 469 states, showing the applicability of the proposed approach.
- An evaluation of the approach on a testbed microgrid consisting of six inverters and a load-bank, showing the practical applicability of the approach on existing hardware.
- A comparison of the approach to other \mathcal{H}_∞ tuning methods, which underlines the significantly faster computation times.

The remainder of this work is organized as follows: Section 2 outlines the problem and derives suitable models. We introduce the proposed structured controller synthesis approach with the stability proof in Section 3. Section 4 presents the simulation studies considering power systems with 10 and 53 power plants. The experimental validation is presented in Section 5, whereas Section 6 shows the computational performance of the approach before providing conclusions in Section 7.

1.1. Mathematical preliminaries

$\bar{\sigma}(\cdot)$ denotes in the following the largest singular value of a matrix, equivalently $\bar{\lambda}(\cdot)$ denotes the largest eigenvalue of a matrix, whereas $(\cdot)^*$ denotes the conjugate transpose of a matrix. The notation $>$ (\geq), and $<$ (\leq) is used to denote positive (semi)definiteness and negative (semi)definiteness of a matrix, respectively. We use j to denote the imaginary unit, $\mathbb{R}_{\geq 0}$ denotes the set of non-negative real numbers, \mathbb{C} denotes the set of complex numbers, and $\mathbb{C}_{>0}$ denotes the set of complex numbers with a positive real part. The notation \mathcal{RH}_∞ is used to denote the set of proper, real rational and stable transfer matrices. Furthermore, we define the operators $<$ (\leq), $>$ (\geq), and $|\cdot|$ element-wise for vectors.

Definition 1. [46] A complex number s_p is a pole of the transfer matrix $G(s) : \mathbb{C} \rightarrow \mathbb{C}^{n_y \times n_w}$, when at least one element $G_{ij}(s)$ of $G(s)$ has a pole at s_p .

We will reference the Bounded real Lemma, which states the following

Lemma 1. (Bounded-real Lemma) [29] Consider the continuous-time transfer function $G(s)$ with the realization $G(s) = D + C(sI - A)^{-1}B$. The following statements are equivalent

- The system $G(s)$ is asymptotically stable and $\|G(s)\|_\infty < \gamma$.
- There exists a symmetric positive definite solution $P > 0$ (Lyapunov matrix) to the linear matrix inequality (LMI)

$$\begin{pmatrix} A^T P + PA & PB & C^T \\ B^T P & -\gamma I & D^T \\ C & D & -\gamma I \end{pmatrix} < 0. \quad (1)$$

2. Optimal Controller Tuning for Power Systems

Figure 1 shows an exemplary power system with the basic idea of retuning controller parameters. It consists of heterogeneous components, such as power plants, renewable generation, storage systems and households. We name these components prosumers, as they can either produce or consume electric power. Thereby, we distinguish between dynamic and static prosumers.

Dynamic prosumers, such as power plants, are dynamic systems with internal states, denoted with \mathcal{P}_i . They possess structured controllers, whose parameters \mathbf{K}_{ti} can be tuned, marked with red in Fig. 1. We consider dynamic prosumers \mathcal{P}_i which control their voltage magnitude V_i and phase θ_i at the point of connection, whereas their power infeed into the grid P_{pi} and Q_{pi} is the external input for the controllers. This is a standard description, e.g. for conventional power plants with synchronous generators [1], as depicted in Fig. 1, where V_i and θ_i are outputs of \mathcal{P}_i , and P_{pi} , Q_{pi} are the inputs. However, the applicability of the modeling is not restricted to this dynamic prosumer type, and dynamic prosumers which have P_{pi} and Q_{pi} as output can also be considered.

Static prosumers, such as loads and some renewable generation, have no internal states and are characterized through their

active and reactive power infeed, denoted with P_{ci} and Q_{ci} , respectively. Figure 1 depicts four static prosumers, marked with blue. We collect infeeds of static prosumers into vectors \mathbf{P}_s and \mathbf{Q}_s , which are considered as external inputs. Renewable generation and loads are often modeled as static prosumers [47, 48]. The power infeed of these elements cannot be fully controlled, and we consider these infeeds as the disturbance inputs for the controller tuning. Static prosumers also model components with a slow dynamic behavior, such as aggregated powers of small prosumers. For this reason, a subset of \mathbf{P}_s and \mathbf{Q}_s is chosen as the disturbance input \mathbf{w}_s . The voltage phasors of buses with static prosumers have a magnitude V_{si} and angle θ_{si} . Static and dynamic prosumers are coupled through the power grid.

Depending on the infeed of renewable generation and load, the system dynamic behavior changes. If the system operator thereby notices that the resiliency of the system decreases, it tunes the controller parameters \mathbf{K}_{ti} of dynamic prosumers in order to increase the system resiliency. The reparameterization process is depicted with red dashed lines in Fig. 1. Thereby, slow communication is needed.

In power systems, the frequencies of the dynamic prosumers, defined with $\omega_i = \dot{\theta}_i$, where θ_i is the angle of the voltage phasor of \mathcal{P}_i , are important and these are typically used to assess the system performance [1]. Thus, choosing the vector of frequencies as the performance output

$$\mathbf{y} = (\omega_1 \quad \dots \quad \omega_N)^T, \quad (2)$$

is a sensible choice. Here N denotes the number of dynamic prosumers, and ω_i is the voltage frequency of \mathcal{P}_i . The performance outputs are marked green in Fig. 1.

In the following subsections, we outline the structure and dynamics of the power grid and prosumers and present possible models.

2.1. Power grid

The power grid consists of power lines, cables, transformers etc. which interconnect dynamic and static prosumers. In principle, each power line and cable, has its own dynamics, which, however, have time constants which are orders of magnitude smaller than the generation dynamics relevant for stability studies, which are often slower than 10 Hz [1]. For this reason, the power grid dynamics are often neglected [49, 1]. Consequently, the grid, i.e. the power flow, is typically described by the algebraic power flow equations

$$P_i = \sum_{j=1}^{N_B} V_{Bi} V_{Bj} (G_{cij} \cos \Delta\theta_{Bij} + B_{sij} \sin \Delta\theta_{Bij}) \quad (3a)$$

$$Q_i = \sum_{j=1}^{N_B} V_{Bi} V_{Bj} (G_{cij} \sin \Delta\theta_{Bij} - B_{sij} \cos \Delta\theta_{Bij}), \quad (3b)$$

where N_B is the number of buses (nodes) in the power system and is equal to the total number of dynamic and static prosumers in the grid, P_i and Q_i are the injected active and reactive powers into the i -th bus (node) in the grid by a dynamic prosumer (P_{pi} , Q_{pi}) or a static prosumer (P_{si} , Q_{si}), V_{Bi} and θ_{Bi} are the magnitude and angle of the voltage phasor at the i -th bus from a dynamic prosumer (V_i , θ_i) or a static prosumer (V_{si} , θ_{si}), and

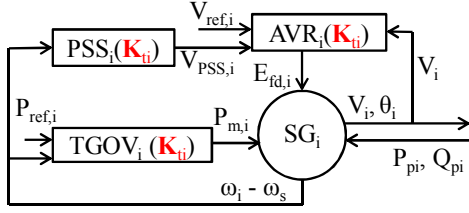


Figure 2: Simplified model of a dynamic prosumer \mathcal{P}_i , a power plant. It consists of a synchronous generator (SG_i), automatic voltage regulator and exciter (AVR_i), power system stabilizer (PSS_i), and of a turbine and governor model (TGOV_i).

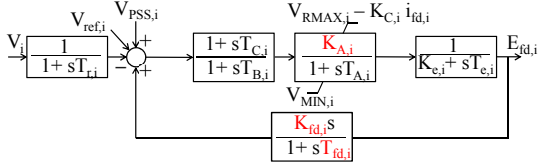


Figure 3: Dynamic model of AVR_i [50], where $T_{r,i}$ is the transducer time constant, $T_{C,i}$ and $T_{B,i}$ are dynamic gain reduction time constants, $K_{A,i}$ is the AVR gain, $T_{A,i}$ is the AVR lag time constant, $K_{e,i}$ and $T_{e,i}$ are the exciter parameters, and $K_{f,d,i}$ and $T_{f,d,i}$ additional damping coefficients of the AVR. We assume that $K_{A,i}$, $K_{f,d,i}$, and $T_{f,d,i}$, marked red, are tunable.

G_{cij} and B_{sij} are the elements of the conductance and susceptance matrix of the grid [1].

As the share of fast, inverter-based generation in power systems increases, algebraic modeling of the power flow is facing increasing scrutiny. Fast control loops of inverters may cause unwanted interactions with power grid dynamics, raising the need for dynamic power flow equations [6]. However, the considered numerical examples, and the testbed microgrid system did not have this issue. Including dynamic power flow equations into the modeling is part of future work.

2.2. Dynamic prosumers and tunable parameters

The proposed structure allows for arbitrary dynamic prosumers. In this section, two exemplary prosumers and their models are outlined.

2.2.1. Power plants

Power plants often consist of a synchronous generator with controllers and actuators, as shown in Fig. 2. We consider the 6-th order model for the synchronous generator (SG_i). For details, we refer the interested readers to [1].

The automatic voltage regulator and exciter (AVR_i) represents hardware and controllers which control the voltage at the power plant terminals V_i as close as possible to a reference value $V_{ref,i}$. The output of AVR_i is the field winding voltage $E_{fd,i}$ which is an input of the SG_i. An exemplary model of an AVR with three tunable parameters, marked red, is shown in Fig. 3. It is important to note that automatic voltage regulators can reduce the stability margin in power systems [1]. For this reason, power plants are sometimes equipped with power system stabilizers (PSS_i). PSSs are analogue or digital controllers, with the task to improve the system stability and increase the damping of oscillations in power systems. An exemplary PSS

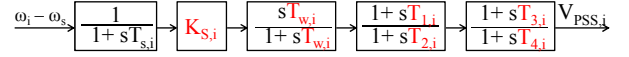


Figure 4: Dynamic model of the simple power system stabilizer (taken from [51, 1]), where $K_{S,i}$ is the PSS gain, $T_{w,i}$ is the washout time constant, $T_{1,i}$ - $T_{4,i}$ are the lead-lag filters time constants, and $T_{s,i}$ is the sensor time constant. All of the PSS parameters are tunable, except the sensor time constant.

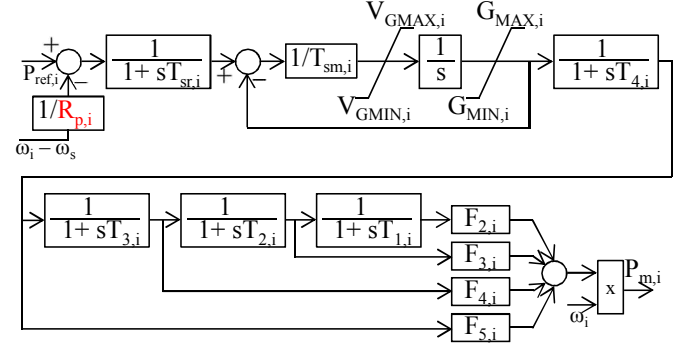


Figure 5: Dynamic model of the turbine and governor from [52]. The frequency droop gain of the governor $R_{p,i}$ is an optimization variable.

is visualized in Fig. 4. The governor and turbine (TGOV_i) control the generator frequency by adapting the mechanical power $P_{m,i}$ transferred to the synchronous generator, see Fig. 5 for an example of a TGOV model with one tunable parameter, marked red. In practice, many different controllers are used, see e.g. [53]. Examples for these controllers are shown in Figs. 3-5, which are used in a subsequent numerical study.

2.2.2. Inverters

We consider inverters which control the voltage and frequency at their terminals, called voltage-source inverters (VSI), or inverters in grid-forming mode. For dynamics below 10 Hz, modeling the high-frequency switching of power transistors in the inverters is often not necessary. Instead, the transistors are approximated as ideal voltage sources with droop controllers for voltage amplitude and frequency, c.f. Fig. 6. The DC link capacitor of the inverters is not considered, as we assume that the internal control of the inverters is fast to compensate for the changes on the DC side. Such simplifications comply with measurements shown in [54], and with the experiments considered in Section 5. Note that the presented inverter model, represent-

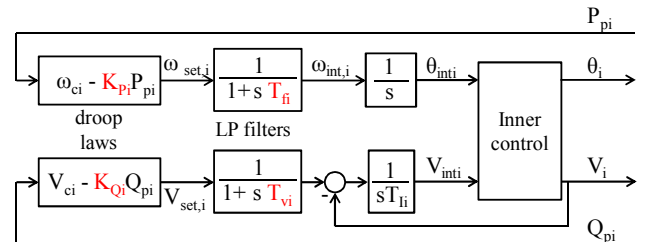


Figure 6: Simplified model of a dynamic prosumer \mathcal{P}_i , an inverter with so-called droop controls.

ing the behavior of a SINAMICS inverter [55], does not have fast inner control in a synchronously rotating frame [6].

In grid-forming mode, the i -th inverter controls the magnitude V_i and phase θ_i of the voltage on its terminals, whereas the active and reactive power infeed of the inverter result from the power flow. The frequency setpoint of the inverter ω_{seti} is determined by the so-called droop equation

$$\omega_{seti} = \omega_{ci} - K_{Pi}P_{pi}, \quad (4)$$

where ω_{ci} is the frequency setpoint with zero load, P_{pi} is the measured active power infeed of the i -th inverter, and K_{Pi} is the frequency droop gain. The setpoint ω_{seti} is filtered with a first-order low-pass filter with the time constant T_{fi} and integrated to obtain the internal voltage phase θ_{inti} . Analogously, the voltage setpoint V_{seti} is determined with the so-called droop equation

$$V_{seti} = V_{ci} - K_{Qi}Q_{pi}, \quad (5)$$

where V_{ci} is the voltage setpoint with no reactive power generation, Q_{pi} is the measured reactive power infeed of the i -th inverter, and K_{Qi} is the frequency droop gain. The setpoint V_{seti} is filtered with a time constant T_{vi} , and serves as the setpoint for the integral voltage controller. The output of the integral controller is the internal voltage V_{inti} .

The resulting θ_{inti} and V_{inti} are used as references to the internal control loops which run at a much higher frequency. As the internal control loops are not modeled due to their fast dynamics, we assume $\omega_i = \omega_{inti}$, $\theta_i = \theta_{inti}$ and $V_i = V_{inti}$.

The tunable inverter parameters are marked red in Fig. 6, they are: $\mathbf{K}_{ti} = (K_{Pi}, K_{Qi}, T_{fi}, T_{vi})^T$. Note that we only tune parameters of the outer control loops, operating on a slower time scale than e.g. current controllers. This, together with the fact that T_{fi}, T_{vi} are restricted to values above 50ms, prevents undesired interactions between inverter control and grid dynamics, enabling the use of algebraic power flow equations in the considered testbed.

2.3. Overall problem setup

Combining the power grid equations (3) with the prosumer models leads to differential-algebraic nonlinear equations

$$\dot{\mathbf{x}} = f(\mathbf{x}, \mathbf{w}, \mathbf{K}_t) \quad (6a)$$

$$0 = h(\mathbf{x}, \mathbf{w}, \mathbf{K}_t), \quad (6b)$$

where $\mathbf{x} \in \mathbb{R}^{N_x}$ combines all dynamic prosumer states, $\mathbf{w} \in \mathbb{R}^{N_D}$ is the vector of disturbance inputs, represented by a subset of \mathbf{P}_C and \mathbf{Q}_C , $\mathbf{K}_t \in \mathbb{R}^{N_t}$ is the vector of tunable controller parameters of all dynamic prosumers, f describes the prosumer dynamics, and h represents the power flow equation (3). We combine the system dynamics (6) with the performance output (2) to obtain the nonlinear model of our power system.

Our goal is to increase of system robustness towards disturbances from \mathbf{w} (a subset of \mathbf{P}_C and \mathbf{Q}_C) and to improve the time domain behavior of the system. For simplicity, we linearize (6) around a known steady-state \mathbf{x}_0 with the known input \mathbf{w}_0 . While this is an approximation, it allows us to use linear systems methods. It has furthermore been shown to be sufficient even for

large-scale disturbances [47]. Moreover, if large disturbances are considered, several linearization points may be used. After eliminating the linearized algebraic equation (6b), we obtain the overall system

$$\dot{\tilde{\mathbf{x}}} = \tilde{A}(\mathbf{K}_t)\tilde{\mathbf{x}} + \tilde{B}(\mathbf{K}_t)\mathbf{w} \quad \mathbf{y} = \tilde{C}\tilde{\mathbf{x}}. \quad (7)$$

The system matrix $\tilde{A}(\mathbf{K}_t)$ has an eigenvalue at zero, as the coupling power flow equation (3) is invariant under phase offsets $\theta_i = \theta_i + \delta\theta$, where $\delta\theta \in \mathbb{R}$ is identical for all i . This zero eigenmode can be eliminated [14], leading to

$$\dot{\mathbf{x}} = A(\mathbf{K}_t)\mathbf{x} + B(\mathbf{K}_t)\mathbf{w} \quad \mathbf{y} = C\mathbf{x}, \quad (8)$$

where $A(\mathbf{K}_t)$ has no parameter-independent eigenvalues on the imaginary axis, and $A(\mathbf{K}_t)$ has all eigenvalues in the left half plane for suitable choice of \mathbf{K}_t . The resulting state space system can be written in the frequency domain as

$$G(\mathbf{K}_t, s) = C(sI - A(\mathbf{K}_t))^{-1}B(\mathbf{K}_t). \quad (9)$$

3. Method for structured \mathcal{H}_∞ parameter tuning

This section defines an optimization algorithm which minimizes the \mathcal{H}_∞ norm of $G(\mathbf{K}_t, s)$, denoted with $\|G(\mathbf{K}_t, s)\|_\infty$, and defined by [56]

$$\|G(s)\|_\infty := \sup_{s \in \mathbb{C}_{>0}} \bar{\sigma}(G(s)) = \sup_{\omega \in \mathbb{R}} \bar{\sigma}(G(j\omega)). \quad (10)$$

Note that the last equality is only valid for stable systems. The \mathcal{H}_∞ norm is chosen, as it represents the maximal amplification of amplitude of any harmonic input signal in any output direction. Thus, minimizing the \mathcal{H}_∞ norm minimizes the worst-case amplification of oscillation frequencies after a disturbance. Thereby, the system robustness is additionally improved. Minimization of $\|G(\mathbf{K}_t, s)\|_\infty$ is achieved by optimizing the vector of tunable parameters \mathbf{K}_t . For notational convenience, we drop writing the dependency on the tunable parameter vector \mathbf{K}_t explicitly, when it is not necessary, and write only $G(s)$. It is assumed, however, that $G(s)$ is always a function of the tunable parameters.

We consider that the system $G(\mathbf{K}_t, s) \in \mathcal{RH}_\infty$ is an asymptotically stable and detectable linear time-invariant multi input multi output (LTI MIMO) system. It has a nonlinear dependency on the vector of tunable controller parameters \mathbf{K}_t .

The basis for the proposed parameter tuning method is the following theorem, which can be found in the literature in analogous forms, see e.g. [43, 27] and references therein.

Theorem 1 (Semi-infinite \mathcal{H}_∞ constraint). *Given a detectable and asymptotically stable system $G(s)$. The \mathcal{H}_∞ norm of $G(s)$ is smaller than $\gamma \in \mathbb{R}$ if and only if*

$$\begin{pmatrix} \gamma I & G(j\omega) \\ G(j\omega)^* & \gamma I \end{pmatrix} > 0, \quad \forall \omega \in \mathbb{R}_{\geq 0}. \quad (11)$$

Proof. Since $\bar{\sigma}(G(j\omega))^2 = \bar{\lambda}(G(j\omega)^*G(j\omega))$, it follows

$$\|G(j\omega)\|_\infty < \gamma \quad (12)$$

$$\Leftrightarrow \bar{\lambda}(G(j\omega)^*G(j\omega)) < \gamma^2, \quad \forall \omega \in \mathbb{R}_{\geq 0} \quad (13)$$

$$\Leftrightarrow G(j\omega)^*G(j\omega) - \gamma^2 I < 0, \quad \forall \omega \in \mathbb{R}_{\geq 0}. \quad (14)$$

By using the Schur complement on the last expression, we obtain (11). \blacksquare

Theorem 1 allows to directly formulate an optimization problem for the \mathcal{H}_∞ minimization of $G(\mathbf{K}_t, j\omega)$

$$\min_{\gamma, \mathbf{K}_t} \gamma \quad (15a)$$

$$\text{s.t.} \quad \begin{pmatrix} \gamma I & G(\mathbf{K}_t, j\omega) \\ G(\mathbf{K}_t, j\omega)^* & \gamma I \end{pmatrix} > 0, \quad \forall \omega \in \mathbb{R}_{\geq 0} \quad (15b)$$

$$\mathbf{K}_{min} \leq \mathbf{K}_t \leq \mathbf{K}_{max}. \quad (15c)$$

The last inequality is a box constraint on the controller parameters, determined by practical considerations or physical constraints. As (15b) needs to be satisfied for every $\omega \in \mathbb{R}_{\geq 0}$, Problem (15) is semi-infinite. This formulation is similar to those considered in [43, 27, 31] and the references therein. One way to find a finite-dimensional approximation to (15) is to use a finite, but large enough, number of frequency samples at which constraint (15b) is evaluated

$$\min_{\gamma, \mathbf{K}_t} \gamma \quad (16a)$$

$$\text{s.t.} \quad \Phi(G(\mathbf{K}_t, j\omega_\mu), \gamma) = \begin{pmatrix} \gamma I & G(\mathbf{K}_t, j\omega_\mu) \\ G(\mathbf{K}_t, j\omega_\mu)^* & \gamma I \end{pmatrix} > 0, \\ \forall \omega_\mu \in \Omega \quad (16b)$$

$$\mathbf{K}_{min} \leq \mathbf{K}_t \leq \mathbf{K}_{max}. \quad (16c)$$

Here Ω is the discrete set of sampled frequencies with N_ω elements. Since the problem scales linearly with N_ω , a reasonably large number of elements in Ω can be chosen such that it covers the required frequency range with satisfactory density [43]. Note that the choice for Ω is problem specific and needs to be adapted to the considered frequency range. With a sufficiently large number of samples in Ω , the local optimum of (16) can be arbitrarily close to the optimum of (15). The advantage of (16) compared to methods based on Lemma 1, with respect to scalability, are severalfold. Approaches based on Lemma 1 introduce a positive-definite (Lyapunov) matrix as an optimization variable, which has the same size as the closed loop system, causing the number of optimization variables to increase quadratically with the number of states in the closed-loop system. Additionally, the size of the matrix in (1) scales linearly with the number of states, inputs, and outputs of the system. Problem (16) does not have the Lyapunov matrix P as an optimization variable, and the size of the problem only depends on the number of inputs and outputs of the system, making the controller synthesis generally faster.

Problems (15) and (16), however, do not guarantee system stability in a straightforward manner, i.e. a controller parameterization obtained as a solution of (16) does not necessarily stabilize the system in addition to minimizing the cost function representing the \mathcal{H}_∞ norm. To overcome this problem, one can introduce constraints based on the Nyquist criterion, c.f. [31, 27], which guarantee closed-loop stability. If the open-loop system, i.e. the system without controllers, is stable, then

the boundedness of the \mathcal{H}_∞ norm of the system sensitivity matrix ensures the stability of the closed-loop system [57, 43].

Remark 1. Note that, even though boundedness of the system \mathcal{H}_∞ norm is a necessary and sufficient condition for system stability, (16) does not guarantee the synthesis of a stable controller parameterization. This is because the last equality in (10) is applicable if and only if $G(s)$ is exponentially stable [56]. We overcome this by providing a suitable stability certificate for the solution of Problem (16).

To this end, we introduce two lemmas and propose a theorem for the stability certificate.

Lemma 2. Given a detectable and exponentially stable system $G(\mathbf{K}_t, s)$ with a fixed parameter vector \mathbf{K}_t and the finite set of poles \mathcal{S}_H . The largest singular value of $G(s)$, denoted with $\bar{\sigma}(G(s))$, approaches $+\infty$ as s approaches any $s_{pij} \in \mathcal{S}_H$, where s_{pij} denotes the p -th pole of the transfer function in the i -th row and j -th column of $G(s)$.

Proof. For clarity of presentation, we present the proof when s_{pij} is a pole with a multiplicity of one. The proof when s_{pij} is a pole with larger multiplicity is analogous. Per definition, we have [58]

$$\bar{\sigma}(G(s)) = \max_{\|\mathbf{z}\|_2=1} \|G(s)\mathbf{z}\|_2. \quad (17)$$

Thus, for all $s_{pij} \in \mathcal{S}_H$

$$\lim_{s \rightarrow s_{pij}} \bar{\sigma}(G(s)) = \lim_{s \rightarrow s_{pij}} \max_{\|\mathbf{z}\|_2=1} \|G(s)\mathbf{z}\|_2 \\ \geq \lim_{s \rightarrow s_{pij}} \|G(s)e_j\|_2, \quad (18)$$

where e_j denotes a column vector where the j -th row is equal to one and all other elements are zero. The last expression can be reformulated to

$$\lim_{s \rightarrow s_{pij}} \|G(s)e_j\|_2 = \lim_{s \rightarrow s_{pij}} \left\| \left(G_{1j}(s) \dots G_{ij}(s) \dots G_{Nj}(s) \right)^T \right\|_2 \\ = \lim_{s \rightarrow s_{pij}} \sqrt{G_{1j}^2(s) + \dots + G_{ij}^2(s) + \dots + G_{Nj}^2(s)}, \quad (19)$$

where $G_{ij}(s)$ denotes the single-input-single-output (SISO) transfer function in the i -th row and j -th column of $G(s)$. Since s_{pij} is a pole of $G_{ij}(s)$, it follows that $\lim_{s \rightarrow s_{pij}} G_{ij}(s)^2 = +\infty$ and that $\lim_{s \rightarrow s_{pij}} \|G(s)e_j\|_2 = +\infty$. From (18), it directly follows that $\lim_{s \rightarrow s_{pij}} \bar{\sigma}(G(s)) = +\infty$. \blacksquare

Lemma 3. Given the linear system $G(\mathbf{K}_t, s)$. If the denominator polynomials in $G(\mathbf{K}_t, s)$ are continuous functions of the controller parameters \mathbf{K}_t , then the location of poles of $G(\mathbf{K}_t, s)$ are also continuous functions of the controller parameters \mathbf{K}_t .

Proof. According to Definition 1, the poles of $G(\mathbf{K}_t, s)$ are obtained as the roots of denominator polynomials of all elements $G_{ij}(\mathbf{K}_t, s)$ of $G(\mathbf{K}_t, s)$. The roots of a polynomial are continuous functions of the polynomial coefficients [59], whereas the denominator polynomial coefficients are continuous functions of the controller parameters. It follows that poles of $G(\mathbf{K}_t, s)$ are continuous functions of \mathbf{K}_t . \blacksquare

Remark 2. In Lemma 3, we make the assumption that denominator polynomials in $G(\mathbf{K}_t, s)$ are continuous functions of the controller parameters \mathbf{K}_t . This assumption is satisfied for almost all practically relevant control elements, such as PID controllers, notch filters, lead-lag filters, washout filters etc. Hence, this assumption does not introduce a significant restriction.

We can now formulate a stability certificate to validate that the closed-loop is stable.

Theorem 2 (Semi-infinite stability certificate). *Given an initial, exponentially stabilizing parameterization $\mathbf{K}_{t,0}$ for the detectable system $G(\mathbf{K}_t, s)$ with the set of poles \mathcal{S}_H . Furthermore, using an iterative solution algorithm which minimizes the value of the cost function of the semi-infinite Problem (15) in each iteration, thereby producing the parameter vector $\mathbf{K}_{t,k}$ in the k -th iteration. Then there exists a sufficiently small step size $\Delta\mathbf{K}$, $\Delta\mathbf{K} \geq |\mathbf{K}_{t,k} - \mathbf{K}_{t,k-1}|$ such that the (local) optimum of (15) exponentially stabilizes G .*

Proof. We first show that the solution algorithm will not allow for poles on the imaginary axis, and afterwards we show that there exists a step size which prevents an unstable parameterization from occurring.

Since $\bar{\sigma}(G(s))$ is a continuous function of s [60], and $\lim_{s \rightarrow s_p \in \mathcal{S}_H} \bar{\sigma}(G(\mathbf{K}_t, s)) = +\infty$ (Lemma 2), there exists $\varphi_{s_p} \in \mathbb{R}_{>0}$, such that for any \mathbf{K}_t , $\mathbf{K}_{t,min} \leq \mathbf{K}_t \leq \mathbf{K}_{t,max}$, the following relation holds

$$|s - s_p(\mathbf{K}_t)| \leq \varphi_{s_p} \Rightarrow \bar{\sigma}(G(\mathbf{K}_t, s)) \geq \max_{\omega \in \mathbb{R}} \bar{\sigma}(G(\mathbf{K}_t, j\omega)). \quad (20)$$

Here φ_{s_p} defines a neighborhood of s_p in which the value of $\bar{\sigma}(G(\mathbf{K}_t, s))$ is greater than $\|G(\mathbf{K}_t, s)\|_\infty$ for any allowed \mathbf{K}_t . Thus, in a (local) optimum, every $s_p \in \mathcal{S}_H$ will have at least the distance φ_{s_p} from the imaginary axis. Otherwise, $\|G(\mathbf{K}_t, s)\|_\infty$ would increase. Furthermore, as $s_p(\mathbf{K}_t)$ is continuous (Lemma 3), a maximal step size $\Delta\mathbf{K}$ exists such that

$$\Delta\mathbf{K} \geq |\mathbf{K}_{t,k} - \mathbf{K}_{t,k-1}| \Rightarrow |s_p(\mathbf{K}_{t,k}) - s_p(\mathbf{K}_{t,k-1})| \leq \varphi_{s_p}. \quad (21)$$

With the previously defined $\Delta\mathbf{K}$, s_p will never cross from the stable to the unstable region, as this would mean that the value $\|G(\mathbf{K}_{t,k}, s)\|_\infty$ would increase in at least one iteration, in which $-\varphi_{s_p} \leq \text{Re}(s_p(\mathbf{K}_{t,k})) < 0$, which is not allowed by the solver. ■

The calculation of the allowed step size vector $\Delta\mathbf{K}$ from (21) is numerically expensive and conservative. To avoid this step, we introduce the following algorithm: if an unstable parameterization $\mathbf{K}_{t,k}$ is obtained, the allowed step size is iteratively multiplied by a scalar $\alpha \in (0, 1)$ until a stable parameterization is obtained. This solution is used in the subsequently proposed algorithm. The previous theorem is valid for the semi-infinite problem (15). In the following theorem, we extend the stability-certificate to discrete sampling.

Theorem 3 (Discrete stability certificate). *Given an initial, exponentially stabilizing parameterization $\mathbf{K}_{t,0}$ for the detectable system $G(\mathbf{K}_t, s)$ with the set of poles \mathcal{S}_H . Furthermore, using an iterative solution algorithm which minimizes the value*

of the cost function of the semi-infinite problem (16) in each iteration, thereby producing the parameter vector $\mathbf{K}_{t,k}$ in the k -th iteration. Then there exists a sufficiently small (vector) step size $\Delta\mathbf{K}$, $\Delta\mathbf{K} \geq |\mathbf{K}_{t,k} - \mathbf{K}_{t,k-1}|$ and a sufficiently big (dense) discrete set Ω such that the (local) optimum of (15) exponentially stabilizes G .

Proof. We only outline the proof due to page limitations. The basic idea is that if the density of sampling frequencies $\omega_\mu \in \Omega$ in the k -th iteration is smaller than $2\varphi_{s_p}$, defined with (20), in the frequency regions around relevant poles, then $\max_{\omega_\mu \in \Omega} \bar{\sigma}(G(\mathbf{K}_{t,k}), j\omega_\mu)$ will increase when a pole approaches the imaginary axis, preventing the pole to become unstable. The detailed proof can be obtained analogously as for Theorem 2. ■

A direct consequence of the previous theorems is that Problem (16) cannot stabilize an unstable system. If the initial parameterization $\mathbf{K}_{t,0}$ is unstable, Problem (16) will not allow unstable system poles to cross the imaginary axis to the stable region. Note that the requirement for an initial stabilizing controller is in accordance to the results presented in [31, 27]. In comparison to [43], the stability guarantee in Theorem 3 is applicable to systems which are open-loop unstable, whereas [43] requires that the open-loop system is stable. For better understanding of the claim of Theorem 3, a small example system is visualized in Appendix A.

Problem (16) is non-convex due to the nonlinear dependency on the controller parameters in $G(\mathbf{K}_t, s)$. In order to solve it with convex solvers, we transform the problem into a series of convex optimization problems by linearizing the parameter dependency of $G(\mathbf{K}_t, s)$. To obtain the linearized transfer matrix in the k -th iteration $G_{L,k}(\mathbf{K}_t, s)$, we linearize $G(\mathbf{K}_t, s)$ around the parameter vector obtained in the previous iteration $\mathbf{K}_{t,k-1}$. The following optimization problem is then solved in each iteration

$$\min_{\gamma, \mathbf{K}_{t,k}} \gamma \quad (22a)$$

$$\text{s.t. } \Phi(G_{L,k}(\mathbf{K}_{t,k}, j\omega_\mu), \gamma) > 0, \forall \omega_\mu \in \Omega \quad (22b)$$

$$\mathbf{K}_{t,min} \leq \mathbf{K}_{t,k} \leq \mathbf{K}_{t,max} \quad (22c)$$

$$|\mathbf{K}_{t,k} - \mathbf{K}_{t,k-1}| \leq \Delta\mathbf{K}, \quad (22d)$$

where Φ is defined in (16), and we define the absolute value element-wise for vectors. Constraint (22d) has two purposes in the optimization algorithm. First, it defines a trust region in which the linearization accuracy in $G_{L,k}(\mathbf{K}_{t,k})$ is preserved. Secondly, by reducing $\Delta\mathbf{K}$, it can be used to reduce the step size if we obtain an unstable system during optimization. The resulting iterative convex optimization algorithm is outlined in Fig. 7. In Step 7, $\Delta\mathbf{K}$ is reduced through multiplication with $\alpha \in (0, 1)$, which serves multiple purposes. Firstly, it is used to satisfy the assumptions of Theorem 3. It ensures that the rise of the system \mathcal{H}_∞ norm, due to the approach of a pole, is captured in the optimization. Secondly, it is used to reduce the ‘‘trust region’’ around the linearization point of the parameter dependency if it is not accurate enough, i.e. if $\|G(\mathbf{K}_{t,k}, s)\|_\infty$ increased, although

- 1: **procedure** STRUCTHINF TUNING($G, \mathbf{K}_{t,0}, \Delta \mathbf{K}, k_{max}$)
- 2: $k = 1$, choose $0 < \alpha < 1$
- 3: **while** $k \leq k_{max}$ or not converged **do**
- 4: $G_{L,k}(\mathbf{K}_t) \leftarrow$ linearize $G(\mathbf{K}_t)$ around $\mathbf{K}_{t,k-1}$
- 5: $\mathbf{K}_{t,k} \leftarrow$ solution of (22).
- 6: **if** $\|G(\mathbf{K}_{t,k}, s)\|_{\infty} \geq \|G(\mathbf{K}_{t,k-1}, s)\|_{\infty}$ or $G(\mathbf{K}_{t,k}, s)$ is unstable **then**
- 7: $\Delta \mathbf{K} \leftarrow \Delta \mathbf{K} \times \alpha$
- 8: Increase the frequency sampling if necessary.
- 9: $\mathbf{K}_{t,k} \leftarrow \mathbf{K}_{t,k-1}$
- 10: **end if**
- 11: $k \leftarrow k + 1$
- 12: **end while**
- 13: **end procedure**

Figure 7: Proposed iterative parameter optimization algorithm.

$\|G_{L,k}(\mathbf{K}_{t,k}, s)\|_{\infty}$ was reduced. In subsequent numerical evaluations the value $\alpha = 0.7$ is used. Step 8 adapts the frequency grid Ω if it is not sufficiently dense, such that Theorem 3 is applicable. To this end, frequencies of unstable poles are added to Ω . By choosing $\Delta \mathbf{K}$ small enough and with sufficient sampling, Theorem 3 guarantees that a stabilizing controller is obtained. Convergence to a local optimum is guaranteed if the initial value is close enough to the (locally) optimal value [61]. Note that the proposed optimization is applicable to arbitrary systems which satisfy the previous assumptions, and not only to electrical networks. However, a large frequency grid Ω should be avoided to reduce computation times.

Problem (22) can be extended to optimize the controller parameters to several system realizations κ by solving the following optimization problem

$$\min_{\gamma, \mathbf{K}_t} \gamma \quad (23a)$$

$$\text{s.t. } \Phi(G_{\kappa}(\mathbf{K}_t, j\omega_{\mu}), \gamma) > 0, \forall \omega_{\mu} \in \Omega_{\kappa}, \kappa = 1 \dots N_s \quad (23b)$$

$$\mathbf{K}_{tmin} \leq \mathbf{K}_t \leq \mathbf{K}_{tmax}, \quad (23c)$$

where N_s is the total number of systems. Such formulations are necessary, e.g. when one parameterization is needed for several system realizations. Problem (23) can be solved analogously with the algorithm in Fig. 7 and is used subsequently in a numerical example.

4. Simulation Studies

We evaluate the proposed method considering two power system models with 10 and 53 power plants, respectively. For the optimization, we use the Matlab toolbox YALMIP [62], together with the solver SeDuMi [63]. We validate the optimization results with nonlinear simulation in the commercial power system simulation software Simscape Power Systems and PSS[®]Sincal, to obtain a practically relevant evaluation.

4.1. The IEEE 39 bus 10 generator model

The first example is a dynamic model of the IEEE 39 bus, and 10 power plant system, which is adopted from [51]. The topology of the power system is shown in Fig. 8. It consists of 10

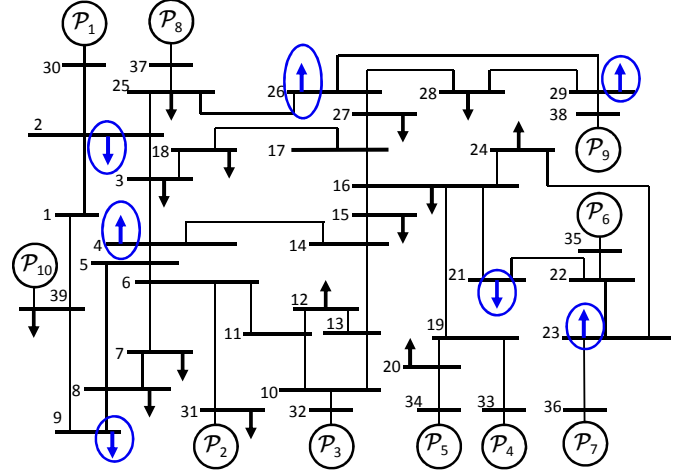


Figure 8: A IEEE 39 bus system with 10 dynamic power plant prosumers [39, 44]. Blue arrows denote the disturbances w_i .

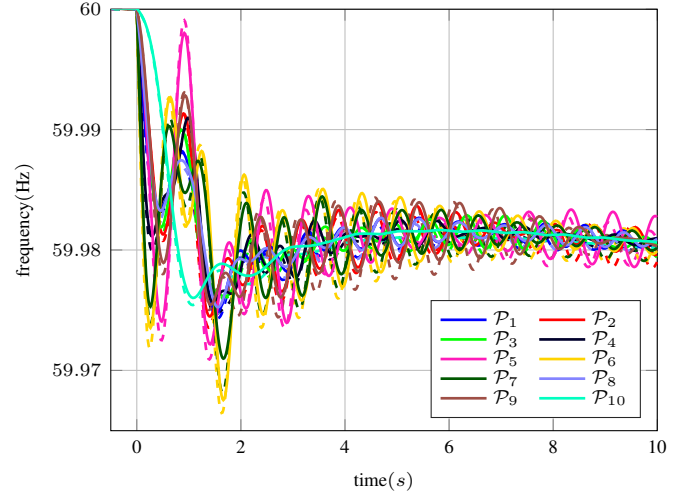


Figure 9: Initial parameters: frequency response after a 100 MW load step in bus 21. Solid lines represent simulations with the nonlinear model, whereas dashed lines represent simulations with the linear model.

power plants whose structure is described in detail in Appendix B. The power system contains static prosumers, denoted with arrows, c.f. Fig. 8. We consider the active powers of constant-power elements in buses 2, 4, 9, 21, 23, 26, 29 as disturbance inputs, marked with blue in Fig. 8. All prosumer and grid parameters are taken from [51]. We increased the exciter gains from 200 to 800 to obtain a stable system. The tunable controller parameters of all power plant controllers are marked red in Figs. 3, 4, and 5. The overall linear system consists of 190 states and 100 tunable controller parameters, c.f. [39, 44]. The initial maximal allowed step size for each controller parameter of each generator is shown in Table A.10 in Appendix B.

Figure 9 shows the linear (dashed lines) and nonlinear (solid lines) simulation of the generator frequencies. The nonlinear simulation is performed in Simscape Power Systems [64] with

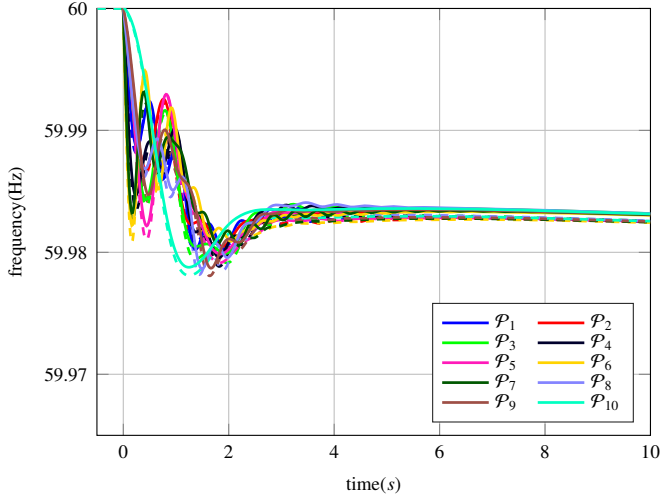


Figure 10: \mathcal{H}_∞ tuned parameters: frequency response after a 100 MW load step in bus 21. Solid lines represent simulations with the nonlinear model, whereas dashed lines represent simulations with the linear model.

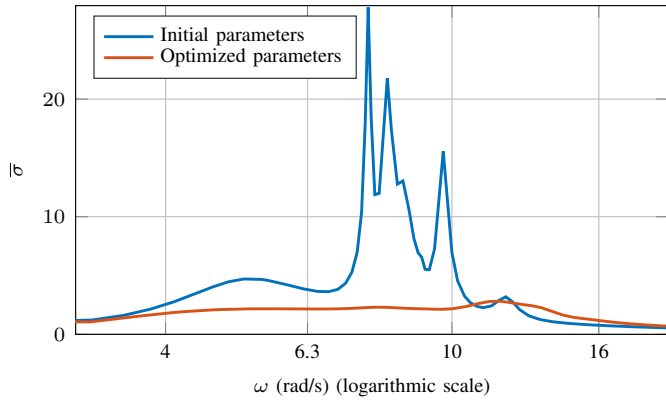


Figure 11: Largest singular value of the linearized IEEE 39 bus power system as a function of frequency ω . After optimization, most of the resonant peaks in the system are eliminated.

nonlinear models of the power plants and the nonlinear power flow. It shows poorly dampened oscillations in the system. Thereby, \mathcal{P}_{10} emulates a connected power system, and thus has a much larger inertia than other power plants. Consequently, its behavior in the time response in Fig. 9 is different than the response of the other power plants. The difference between the linear and nonlinear responses in Fig. 9 is small and the linear model can be utilized for the optimization.

Figure 10 shows the time-domain response using the proposed tuning algorithm, which is significantly improved. Simulations with the optimized parameters of the linear model (dashed lines) again shows good correspondence to the detailed nonlinear simulation (solid lines). The structured controller synthesis reduced the \mathcal{H}_∞ norm by a factor of 10. Thus, the optimally tuned parameters reject disturbances significantly better than in the untuned case. The largest singular value of the system, presented in Fig. 11 as a function of the input frequency,

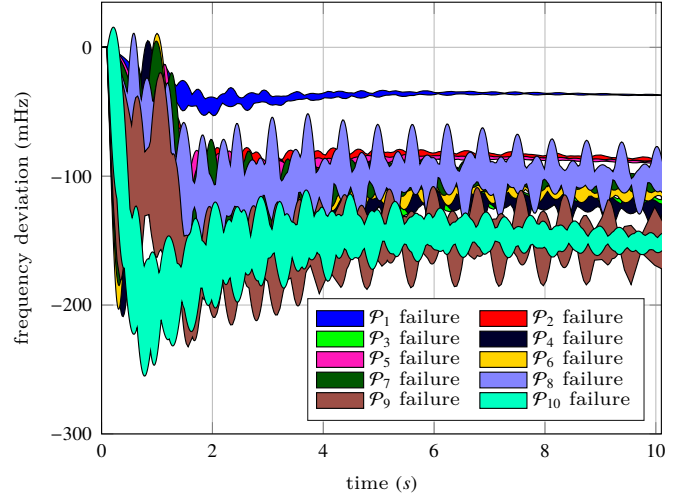


Figure 12: Bounds of nonlinear frequency responses after dynamic prosumer failures with the initial parameterization. Each area shows the response of the remaining 9 dynamic prosumers. The figure shows ten independent nonlinear simulations.

shows that the resonant peaks were practically eliminated after the parameter optimization.

To further demonstrate the efficiency of the proposed approach, we optimize controller parameters considering independent (one-by-one) failures of all dynamic prosumers in the system, as well as the independent failures of power lines (PLs) between buses 2 and 3, 5 and 6, 6 and 11, 21 and 22, 23 and 24, as well as 28 and 29, denoted with PL 1-6, respectively. Such failures excite simultaneous changes of active- and reactive power. Furthermore, as failures occur almost instantaneously in the system, one controller parameterization is needed for all considered failures as there is not enough time to reparameterize the system after a failure. For this purpose, we apply the approach from [65] to convert such failures into equivalent static prosumers. The obtained model, however, is only valid for one considered failure. Hence, we obtain 16 independent systems, for which we find one controller parameterization by using (23). Figure 12 shows the results of 10 simulations using the nonlinear model for the initial parameters. Each shaded area shows the frequency response of the system after the dropout of one prosumer. Thereby, the bounds of the frequencies of the remaining 9 dynamic prosumers is shown. It shows prevailing oscillations in the system after the failure of almost any prosumer. Figure 13 shows 10 simulations after the independent dropout of each dynamic prosumer with the nonlinear model for optimized parameters, demonstrating a significantly improved response, with a reduced overshoot and settling time in all cases. Analogously, Fig. 14 shows the result of six nonlinear simulations with initial parameters. Thereby, each shaded area shows the response of all 10 dynamic prosumers to the considered PL failure. Using the proposed approach, the response of the system to such failures is significantly improved, c.f. Fig. 15.

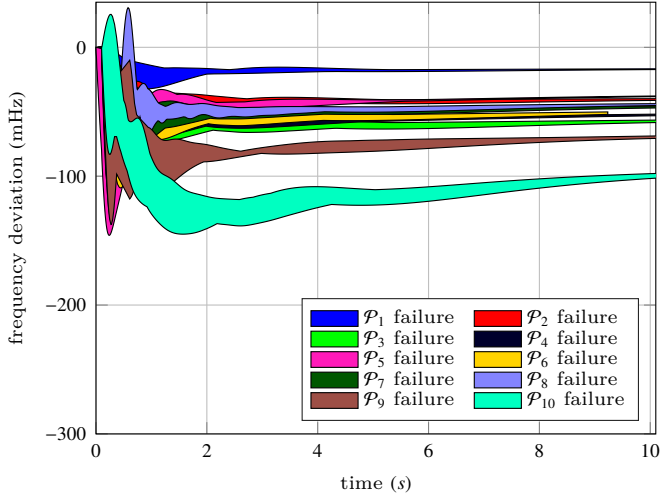


Figure 13: Bounds of nonlinear frequency responses after dynamic prosumer failures with the optimized parameterization. Each area shows the response of the remaining 9 dynamic prosumers. The figure shows ten independent nonlinear simulations.

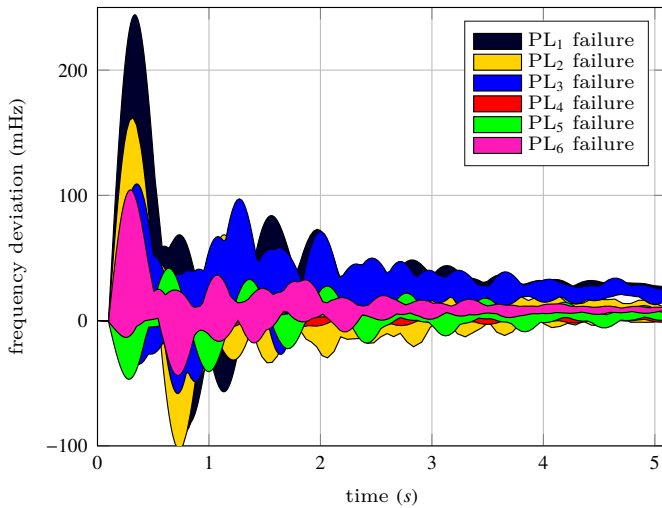


Figure 14: Bounds of frequency responses after power line failures with the initial parameterization. Each area shows the response of all 10 dynamic prosumers. The figure shows six independent nonlinear simulations.

4.2. European 53 generator model

For the second example, we use a model with 53 power plants. It represents a reduced version of the European power system, developed as a part of the research project DynaGrid-Center [66]. An overview of the power system structure is shown in Fig. 16. The grid consists of 35 buses (nodes), connected by long power lines. The controllers used for this model are presented in Appendix C. A more detailed description of the considered system is avoided as it is not necessary for the understanding of the presented results. Nineteen power plants in the system have controllers, whereas all other power plants have a constant exciter voltage $E_{fd,i}$ and turbine mechanical power $P_{m,i}$. The described power system has a total of 469

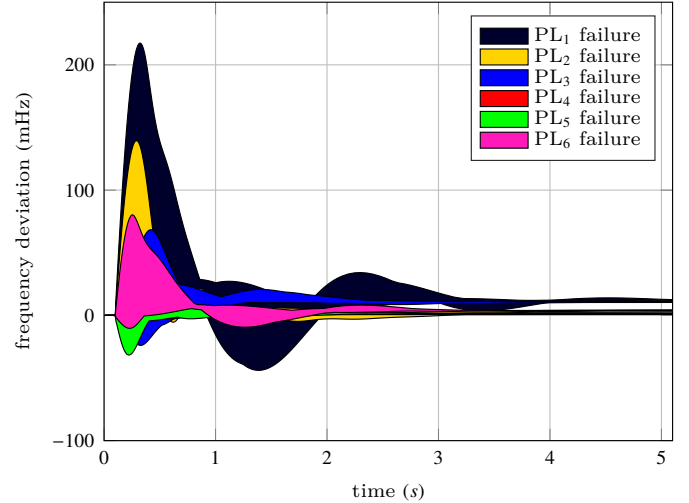


Figure 15: Bounds of frequency responses after power line failures with the initial parameterization. Each area shows the response of all 10 dynamic prosumers. The figure shows six independent nonlinear simulations.

states and 116 controller parameters. We consider the active powers of static prosumers in 15 buses as disturbance inputs, marked with blue in Fig. 16.

Figure 17 shows the frequency response at ten nodes in the system with initial system parameters after a 1.5 GW generation dropout in bus 1. The simulation is done with nonlinear power plant and power grid models in the commercial power system simulation software PSS[®]Sincal. As shown in Fig. 17, poorly damped oscillations are present in the system. The initial parameters were obtained manually with iterative simulation. Due to the system complexity and time limitations, we did not find a better parameterization manually. The proposed tuning algorithm provides a systematic way to tune the parameters of such complex systems.

Figure 18 shows the frequency response after the application of the \mathcal{H}_∞ tuning algorithm. It shows a reduction in the overshoot, as well as significantly improved oscillation damping, confirmed by the singular value plot in Fig. 19. The system \mathcal{H}_∞ norm was reduced by a factor of 5.4, and thereby most of the resonant peaks were practically eliminated; c.f. Fig. 19, even though the parameters of only 19 power plants, from a total of 53, were optimized.

4.3. Discussion

We performed simulation studies on two power system models exploiting linearized models for the tuning and using nonlinear simulation environments for verification. The \mathcal{H}_∞ tuning algorithm reduced the \mathcal{H}_∞ norm of the systems to 0.01% and 19% of the initial norm with static prosumers as disturbances, thereby significantly reducing the time-domain settling time and overshoot of those systems, as summarized in Table 1. The presented approach provides a systematic solution and shows very good results for parameter tuning in these complex systems. The outcomes of the optimization are also validated in commercial power system simulation software with

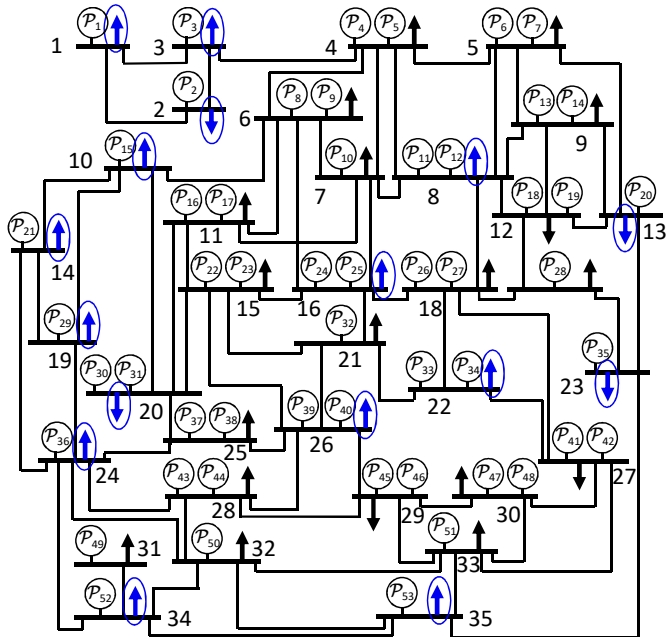


Figure 16: The 53 power plant power system developed in the DynaGridCenter project [66]. Buses with uncertain infeeds, denoting disturbances w_i , are marked blue.

Table 1: Comparison of the \mathcal{H}_∞ norm, settling time, and overshoot improvement for the two power system simulation studies with static prosumers as disturbances.

relation	$\frac{x_{\text{opt}}}{x_{\text{initial}}}$	\mathcal{H}_∞ norm	Settling time	Overshoot
IEEE 39 bus	0.1	0.72	0.66	
European	0.19	0.11	0.78	

detailed nonlinear component models, showing the applicability of the approach to practical systems.

5. Experimental validation

The \mathcal{H}_∞ tuning algorithm was furthermore validated on a testbed microgrid in Wildpoldsried, Germany, as a part of a funded research project [67].

The considered part of the grid consists of six 55 kVA SINAMICS inverters, connected to three Lithium-Ion batteries, and a controllable 150 kW load bank, c.f. Fig. 20. The microgrid can operate attached to the supply grid, as well as in islanded operation. Further details can be found in [67, 54]. We consider the case when the microgrid is running independently of the supply grid. All inverters are running in grid-forming mode, i.e. they control their voltage magnitude and frequency based on their active and reactive power infeed, as shown in Fig. 6. This leads to increased reliability and power quality in the system, because failure of one inverter will not cause a blackout when properly configured. In order to enable parallel operation of the inverters, droop control of active and reactive power is used, as described in Subsection 2.2. Droop control

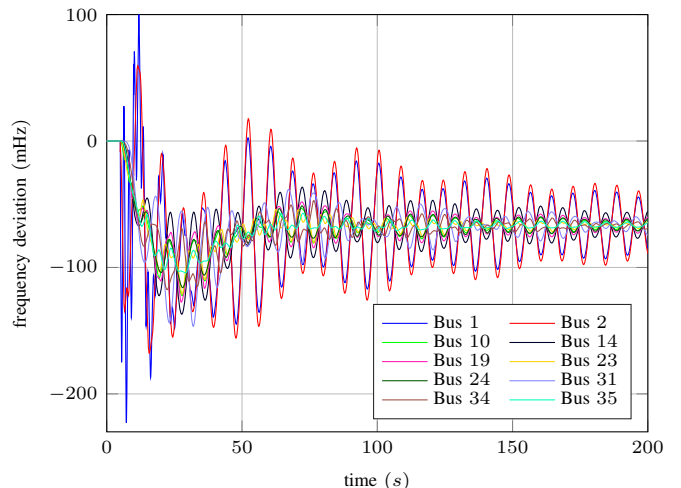


Figure 17: Frequency response in several buses in the system after a 1.5 GW generator outage in bus 1 with initial parameters.

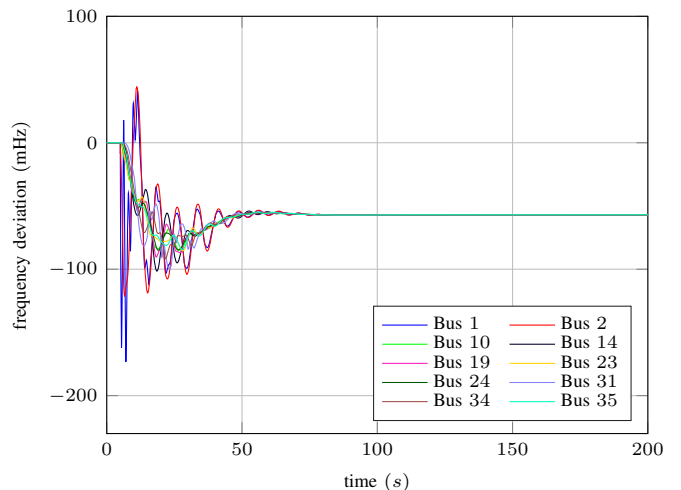


Figure 18: Power plant frequency response after a 1.5 GW load step in bus 1 with \mathcal{H}_∞ tuned parameters.

is the current state-of-the-art method for control of distributed generations for several reasons: it requires only local measurements and no real-time communication or accurate time synchronization, it enables power sharing and parallel operation of grid-forming inverters etc. Other control schemes for inverters, beside droop control, are also possible, such as virtual oscillator control [68] or the virtual synchronous generator concept [69]. We perform load steps with the load bank in order to evaluate the system performance.

The presented system is of interest for several reasons:

- To avoid circulating currents, two isolating transformers are a part of the system, as shown in Fig. 20, which are sources of asymmetry in the load-step response of the inverters. Such asymmetry will also occur if the inverters are geographically distributed within a microgrid. There-

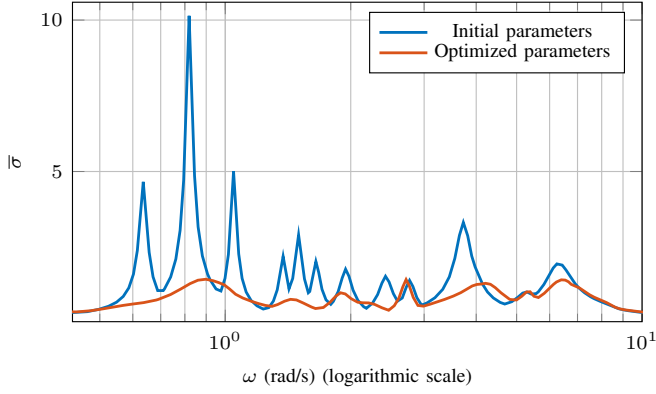


Figure 19: Largest singular value of the linearized reduced European power system model as a function of frequency ω . After optimization, most of the resonant peaks in the system are practically eliminated.

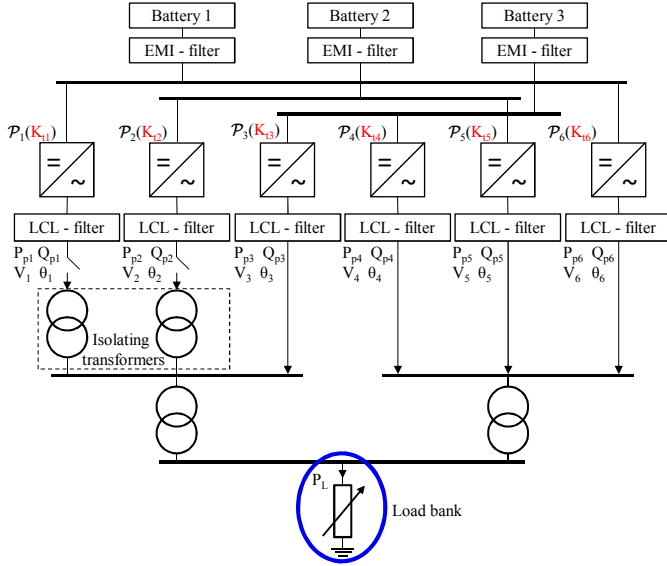


Figure 20: Structure of the considered part of the microgrid, consisting of six parallel connected inverters. Details can be found in [54]. The active power of the load bank, denoted with P_L , is the disturbance input w_i into the system.

fore this configuration is a good test example for a real life setup.

- The system does not have any generation with mechanical inertia. Hence, it is an interesting example for a zero-inertia system.

5.1. Manual tuning of the testbed system

Manual tuning of the system was performed with iterative simulation methods based on the inverter model described in Subsection 2.2, see Fig. 6. The step response in Fig. 21 is obtained with the parameters from Table 2. It shows good correspondence between measurement (solid lines) and simulation (dashed lines), demonstrating the validity of the used model. The difference between measurement and simulation

Table 2: Stable manual parameterization of inverters 1 and 6.

Inv	K_P (%)	K_Q (%)	T_f (ms)	T_v (ms)
1	2	3.1	100	100
6	2	3.1	100	100

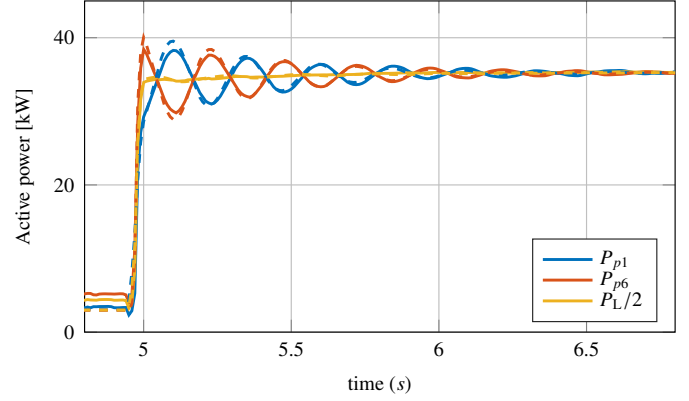


Figure 21: Response to a 60 kW load step with inverters 1 and 6 achieved by manual tuning; P_L is calculated as the sum of P_{p1} and P_{p6} . Solid lines represent measurements, whereas dashed lines represent simulations with the nonlinear model.

originates from unmodeled loads, other inverter controllers, phase-asymmetries etc. We show active power plots, because in this system, the oscillations are better visible in the active power than in the frequencies.

The same parameters from Table 2 are also used for the operation of all six inverters, resulting in the 150 kW load step response shown in Fig. 22. A discrepancy is present in the oscillation frequency between measurement and simulation of inverter 3. A better match can be obtained by an iterative adaptation of grid parameters, i.e. impedances in the grid. We avoid this because mismatches between measurements and simulation are expected in real systems, and as it allows to test the sensitivity of the proposed method to model discrepancies. The setup with six inverters was also used for successful operation with household consumers in islanded mode.

5.2. Automatic tuning of the testbed system

The results obtained by manual tuning in Figs. 21 and 22 show prevailing oscillations in the system after a load step. Arguably, they are still satisfactory for many applications. However, manual tuning requires expert know-how of the system and is associated with a significant time-effort. Automatic tuning methods enable the fast design of robust microgrids, without expert knowledge. We apply and experimentally validate the proposed \mathcal{H}_∞ tuning method on the testbed system.

5.2.1. Parameter tuning for inverters 1 and 6

We first apply the \mathcal{H}_∞ parameter tuning algorithm to the system when only inverters 1 and 6 are running. The response for a 60 kW load step with optimized parameters, c.f. Table 3, is

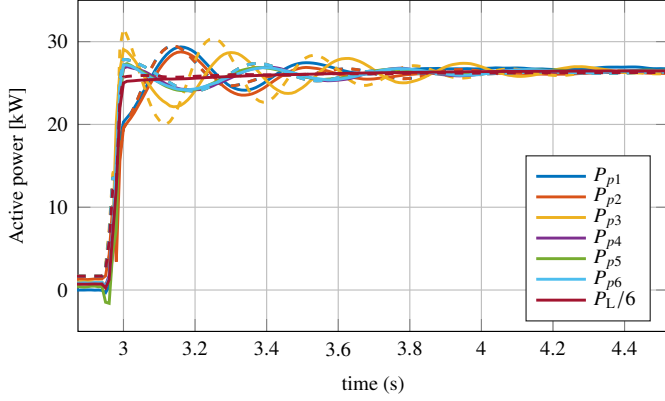


Figure 22: Response to a 150 kW load step with all inverters achieved by manual tuning; P_L is calculated as the sum of all inverter powers. Solid lines represent measurements, whereas dashed lines represent simulations with the nonlinear model.

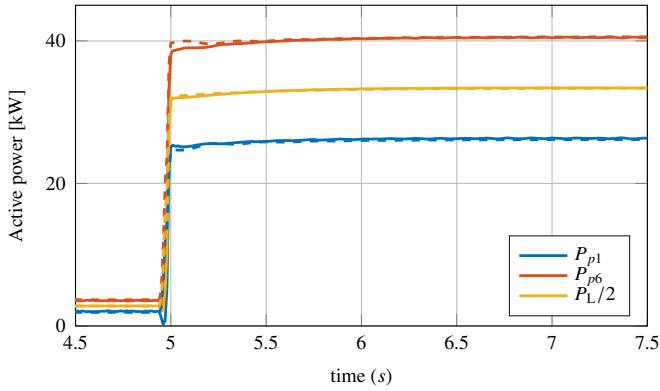


Figure 23: Response to a 60 kW load step with inverters 1 and 6 achieved by optimal tuning of all parameters; P_L is calculated as the sum of P_{p1} and P_{p6} . The optimized parameters are shown in Table 3. Solid lines represent measurements, whereas dashed lines represent simulations with the nonlinear model.

shown in Fig. 23. The settling time of the step response is practically reduced to zero. Measurements with several load steps are shown in Fig. 24, demonstrating that the linear model is valid for a range of loading conditions and disturbances. However, due to different droop values of $K_{P,1}$ and $K_{P,6}$, the steady state power of the inverters is not identical. Such parameterization may cause inverter 6 to overload after a large load step. Still, if the inverters have sufficient power reserves, and no large sudden load changes are expected, this parameterization provides the best step response with regard to oscillation suppression. The generation of the inverters can be balanced out with slower control schemes, called secondary control, which are a standard part of power system control. As they operate at a slower time scale than the ones observed here, they are beyond the scope of this work.

In order to eliminate the generation imbalance even without secondary control, we introduce additional constraints which enforce the equality of the droop gains, i.e. $K_{P1} = K_{P6}$ and

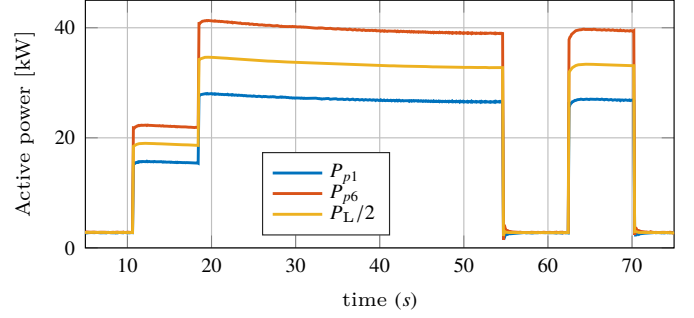


Figure 24: Response of inverters 1 and 6 to 30 and 60 kW load steps with parameters from Table 3.

Table 3: Optimal parameterization of inverters 1 and 6 when all parameters are optimized.

Inv	K_P (%)	K_Q (%)	T_f (ms)	T_v (ms)
1	3.13	3.56	108	104
6	2	3.62	115	104

$K_{Q1} = K_{Q6}$. With these constraints, we obtain optimized parameters shown in Table 4, which achieve the step response shown in Fig. 25. We see that, even with the equality constraint, improvement in the step response of the system is still possible, compared to manual tuning results.

5.2.2. Parameter tuning for all inverters

All 6 inverters are operating in parallel in grid-forming mode. The 150 kW load step response when all tunable inverter parameters are optimized, is shown in Fig. 26. The optimized parameters are shown in Table 5. In this case, the oscillations could not be completely eliminated because of insufficient freedom in the parameterization. Still, a noticeable improvement is observable compared to manual tuning, c.f. Fig. 22.

To avoid unequal power sharing, equality constraints for the droop gains are introduced, i.e. $K_{P,1} = K_{P,2} = \dots = K_{P,6}$ and $K_{Q,1} = K_{Q,2} = \dots = K_{Q,6}$. The step response for this case is shown in Fig. 27, and the obtained parameters in Table 6. The overshoot in this case cannot be avoided. However, the power oscillations after the initial overshoot are reduced when compared to the manual tuning results in Fig. 22.

Summarizing, the results show a good match between measurements and the inverter models. Even though the manual tuning results, as shown in Figs. 21 and 22, are satisfactory for many applications, the results obtained with the proposed parameter tuning algorithm, shown in Figs. 21 - 27, are bet-

Table 4: Optimal parameterization of inverters 1 and 6 with droop equality constraints.

Inv	K_P (%)	K_Q (%)	T_f (ms)	T_v (ms)
1	2	3.13	89	100
6	2	3.13	130	100

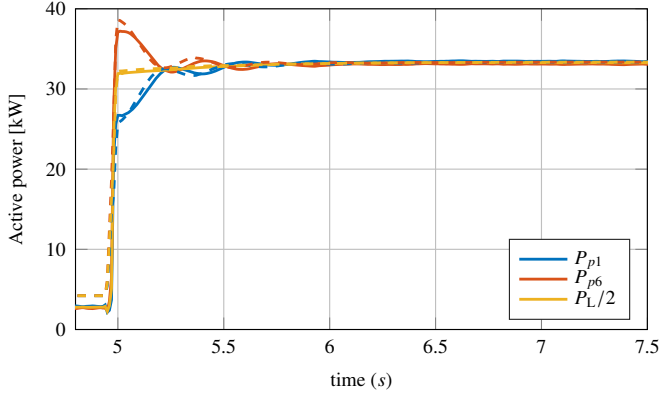


Figure 25: Response to a 60 kW load step with inverters 1 and 6 achieved by optimal tuning together with droop gain equality constraints; P_L is calculated as the sum of P_{p1} and P_{p6} . The optimized parameters are shown in Table 4. Solid lines represent measurements, whereas dashed lines represent simulations with the nonlinear model.

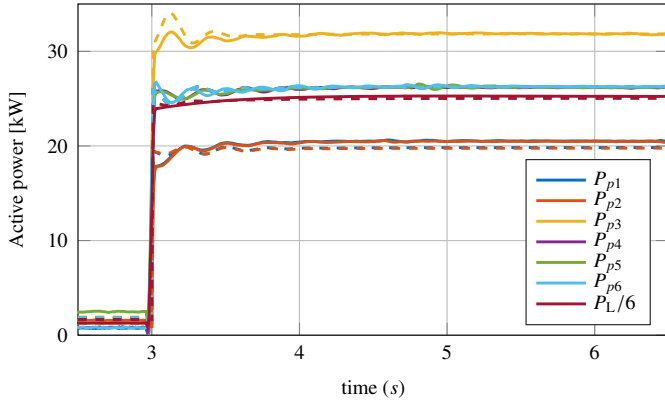


Figure 26: Response to a 150 kW load step with all inverters achieved by optimal tuning of all parameters; P_L is calculated as the sum of all inverter powers. The optimized parameters are shown in Table 5. Solid lines represent measurements, whereas dashed lines represent simulations with the nonlinear model.

ter with respect to oscillation damping. Additionally, no expert knowledge is necessary for the automatic parameterization, and the parameterization process can be done in less time than by manual tuning.

6. Performance comparison

In this section, we focus on the computational efficiency of methods considering structured \mathcal{H}_∞ controller synthesis. For this purpose, we adapt five methods from literature to the considered application. Thereby, we observe the computation time of these methods on several numerical examples. An additional comparison is presented in [70], where the focus of the comparison is on the deliverable results in the time- and frequency domain, observed on an exemplary numerical example. We use for the comparison a Windows computer with an Intel[®] i7-4810MQ CPU running at 2.8 GHz and with 8 GB of RAM. Note that the presented times should only give a hint about the

Table 5: Optimal parameterization of inverters 1 and 6 with no droop equality constraints.

Inv	K_P (%)	K_Q (%)	T_f (ms)	T_v (ms)
1-2	3.1	3.3	107	105
3	2	3.5	124	104
4-6	2.1	3.6	102	104

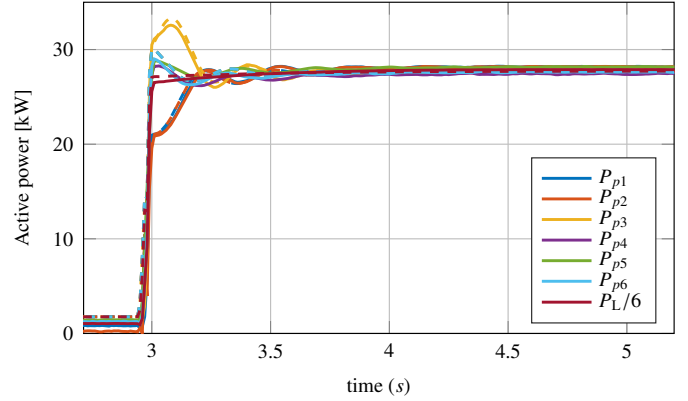


Figure 27: Response to a 150 kW load step with all inverters 1 and 6 achieved by optimal tuning and droop equality constraints; P_L is calculated as the sum of all inverter powers. The optimized parameters are shown in Table 6. Solid lines represent measurements, whereas dashed lines represent simulations with the nonlinear model.

computational complexity, as more tailored methods would allow to further decrease the computation time.

The comparison is done with respect to the computation times, achieved \mathcal{H}_∞ norm, as well as scalability. For this purpose we consider the PK-iteration [39], path-following method [32], linearized convex-concave decomposition [34], non-smooth optimization from the systune toolbox in MATLAB [71], and the projection approach from [42]. Thereby, we expand these methods to be applicable to nonlinear parameter dependencies. Other methods, which assume a static output feedback formulation of the problem, such as cone complementarity linearization and sequential linear programming matrix method [37, 38] are not included in the comparison, as they introduce transformations only applicable to specific linear parameter dependencies.

We begin the comparison with a small system with two power plants, 28 states and 16 optimization parameters. The system is obtained by taking the four power plant grid from [1], disconnecting two power plants, and by dividing the load in

Table 6: Optimal parameterization of inverters 1 and 6 with droop equality constraints.

Inv	K_P (%)	K_Q (%)	T_f (ms)	T_v (ms)
1-2	2	3.1	86	96
3	2	3.1	154	101
4-6	2	3.1	123	100

Table 7: Comparison of structured \mathcal{H}_∞ synthesis methods on a system with two power plants, 28 states and 16 optimization parameters. The initial \mathcal{H}_∞ norm of the system is 23.

method	\mathcal{H}_∞ norm	comp. time	out. iter
Frequency samp.	0.48	6 s	3
PK iter.	0.72	83 s	50
Path-following	1.1	29 s	16
Convex-concave decomposition	0.83	112 s	50
<i>systune</i>	0.42	31 s	NA
Projection method	4.8	1300 s	7

Table 8: Comparison of structured \mathcal{H}_∞ synthesis methods on a system with four power plants, 56 states and 32 optimization parameters. The initial \mathcal{H}_∞ norm of the system is 11.5.

method	\mathcal{H}_∞ norm	comp. time	out. iter.
Frequency samp.	0.56	27 s	5
PK iter.	0.65	670 s	50
Path-following	1.9	640 s	50
Convex-concave decomposition	1.18	1264 s	50
<i>systune</i>	0.27	687 s	NA

half. The initial \mathcal{H}_∞ norm of the system is 23. The grid $\Omega = \{\omega_k | \omega_k = 4 + 0.1 \cdot (k - 1), k = 1 \dots 31\}$ is chosen for the frequency sampling method. Table 7 summarizes the comparison results for this system. All methods improved the system \mathcal{H}_∞ norm. Thereby, the *systune* toolbox, deploying non-smooth optimization, achieves the smallest \mathcal{H}_∞ norm. The frequency sampling method achieves a similar norm, but in 20% of time *systune* required. They are followed by the PK iteration, which achieves a similar system norm as the convex-concave decomposition, but in 75% of the time. The path-following method achieves a worse system norm, but with the second-fastest time. With the projection method, the obtained system norm is the largest, and, even on the small system, the optimization time is over 20 minutes. This is due to the necessity for an eigenvalue decomposition in every step in the inner optimization in one iteration. Since our goal is to find scalable optimization methods, we do not consider the projection method in larger examples.

The second example is the four power plant system from [1]. This system has 56 states, 32 optimization parameters, and an initial \mathcal{H}_∞ norm of 11.5. Table 8 summarizes the results with the considered methods. Again, *systune* achieved the smallest \mathcal{H}_∞ norm of the system, reducing the norm to approx. 2.3% of the initial value. The frequency sampling method, using the same frequency grid as in the previous example, achieved similar results by reducing the system norm to 4.9% of the initial value, but with a 25 times faster computation time. The PK iteration achieves the third-best \mathcal{H}_∞ norm, with a computation

Table 9: Comparison of structured \mathcal{H}_∞ synthesis methods on the IEEE 39 bus system with ten power plants, 190 states and 100 optimization parameters. The initial \mathcal{H}_∞ norm of the system is 27.7.

method	\mathcal{H}_∞ norm	comp. time	out. iter.
Frequency samp.	2.33	266s	4
PK iter.		3800s	
		per iter.	
Path-following		8257s	
		per iter.	
Convex-concave decomposition		13700s	
		per iter.	
<i>systune</i>		out of memory	

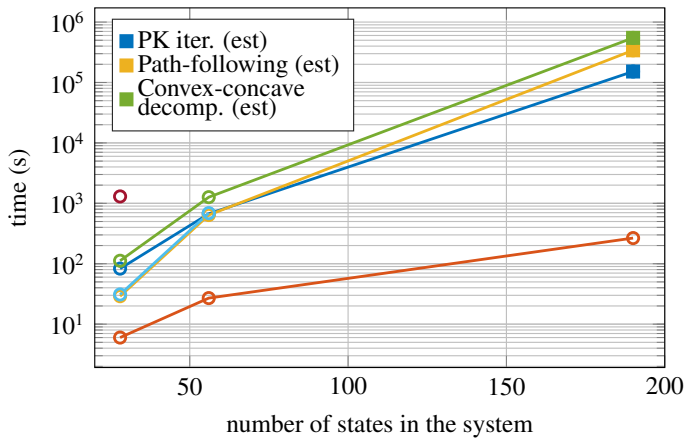
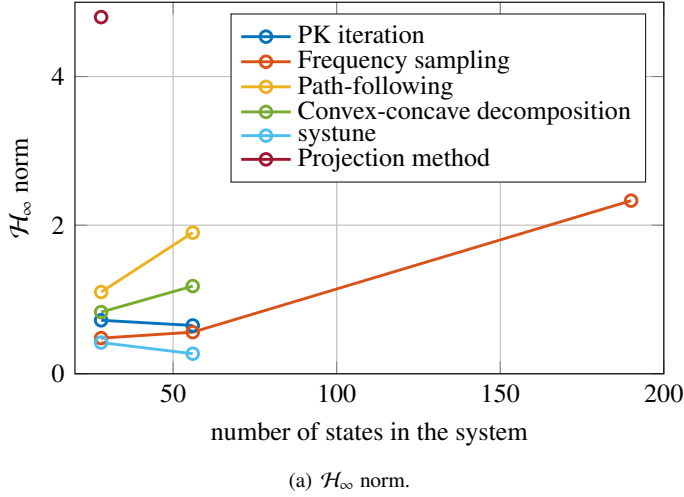
time similar to *systune*.

The third considered example is the ten power plant system from Appendix B, consisting of 190 states and 100 controller parameters. For this system, most of the methods reach the limit for practically tolerable computation times. The tuning with *systune* could not be done due to an "out of memory" error. The optimization results are shown in Table 9. The PK iteration, path-finding, and convex-concave decomposition have large computation times due to the presence of the Lyapunov matrix, whose size scales quadratically with the number of states. For this system, the total computation time for these methods is in the range of one to several days. Only the frequency sampling method was able to find a solution in reasonable time by using the grid $\Omega = \{0.01, 3, 4, 5, 6\} \cup \{\omega_k | \omega_k = 7 + 0.1 \cdot (k - 1), k = 1 \dots 81\}$. Thereby, the density of the grid was increased in the frequency interval with resonant peaks, shown in Fig. 11.

Figure 28(a) summarizes the obtained \mathcal{H}_∞ norms from the previous tables. It shows that the proposed frequency sampling method is only partially outperformed by *systune* for the 4-power plant system. However, it is the only one capable of tuning the parameters of the 10-power plant system in reasonable time. A summary of the computation times for the different methods is shown in Fig. 28(b). Thereby, squares in the plot represent estimated times obtained by multiplying the computation time per iteration from Table 9 with the number of iterations from the smaller systems. It shows that the frequency sampling method achieves orders-of-magnitude smaller computation times, while being only behind *systune* with respect to the achieved \mathcal{H}_∞ norm. However, the performance of the frequency sampling is dependent on the size of the frequency grid. It is important to choose the smallest grid that covers the necessary frequency area with sufficient density. This, however, was not a problem for the considered systems.

7. Conclusions

Tuning of existing controller parameters to reject disturbances in power systems, resulting in oscillations, allows to accommodate changing power system dynamics, e.g. due to an increasing share of renewable generation. Automatic tuning algorithms could allow the system operator to retune the pa-



(b) Computation times. Squares represent estimated times.

Figure 28: Comparison of computation times and achieved \mathcal{H}_∞ norms for the different methods.

rameters of the existing controllers to account for changes and disturbances. We proposed an algorithm for structured \mathcal{H}_∞ controller synthesis and applied it in simulations and experiments to power systems. We proved that the proposed algorithm will produce stabilizing controller parameters given an initial stabilizing controller. We applied the \mathcal{H}_∞ optimization method in two simulation studies containing power systems with 10 and 53 generators. In both cases, the \mathcal{H}_∞ norm of the systems was reduced by more than a factor of five, while the time-response to disturbance steps was also improved. Furthermore, we experimentally evaluated the approach on a testbed islanded microgrid. As shown, the used inverter model corresponds well to measurements. Furthermore, the developed tuning method leads to much better results than one achieves by existing manual tuning, with less time and a reduced amount of necessary expert knowledge of the system. Finally, we compared the proposed approach to others from the literature to demonstrate the scalability of the proposed approach. Future work will focus on more detailed inverter models, as well as including power grid dynamics in the power grid model.

References

- [1] P. Kundur, Power System Stability and Control, McGraw-Hill, 1993.
- [2] entsoe, Analysis of CE inter-area oscillations of 1st december 2016, https://docstore.entsoe.eu/Documents/SOC%20documents/Regional_Groups_Continental_Europe/2017/CE_inter-area_oscillations_Dec_1st_2016_PUBLIC_V7.pdf (December 2020).
- [3] REN21, Renewables 2018 global status report, <http://www.ren21.net/gsr-2018/> (Jan 2020).
- [4] S. Al Ali, T. Haase, I. Nassar, H. Weber, Impact of increasing wind power generation on the north-south inter-area oscillation mode in the European ENTSO-E system, IFAC Proceedings Volumes 47 (3) (2014) 7653–7658.
- [5] A. Crivellaro, A. Tayyebi, C. Gavriluta, D. Groß, A. Anta, F. Kupzog, F. Dörfler, Beyond low-inertia systems: Massive integration of grid-forming power converters in transmission grids, arXiv preprint arXiv:1911.02870 (2019).
- [6] O. Markovic, U. and Stanojev, E. Vrettos, P. Aristidou, G. Hug, Understanding stability of low-inertia systems arxiv.org/jwzrq (Feb 2019).
- [7] A. Mešanović, U. Münz, R. Findeisen, Scalable and data privacy conserving controller tuning for large-scale power networks, submitted, arXiv preprint arXiv:1911.01499 (2019).
- [8] M. Raoufat, K. Tomovic, S. Djouadi, Virtual actuators for wide-area damping control of power systems, IEEE Trans. Power Systems 31 (6) (2016) 4703–4711.
- [9] Y. Pipelzadeh, N. Chaudhuri, B. Chaudhuri, T. Green, Coordinated control of offshore wind farm and onshore HVDC converter for effective power oscillation damping, IEEE Trans. Power Systems 32 (3) (2017) 1860–1872.
- [10] C. Zhu, M. Khammash, V. Vittal, W. Qiu, Robust power system stabilizer design using \mathcal{H}_∞ loop shaping approach, IEEE Trans. Power Systems 18 (2) (2003) 810 – 818.
- [11] G. Befekadu, I. Erlich, Robust decentralized structure-constrained controller design for power systems: an LMI approach, in: Power Systems Computation Conference, 2005.
- [12] M. Mahmoudi, J. Dong, K. Tomovic, S. Djouadi, Application of distributed control to mitigate disturbance propagations in large power networks, in: North American Power Symposium (NAPS), IEEE, 2015.
- [13] R. Preece, J. Milanovic, A. M. Almutairi, O. Marjanovic, Damping of inter-area oscillations in mixed AC/DC networks using WAMS based supplementary controller, IEEE Trans. Power Systems 28 (2) (2013) 1160–1169.
- [14] X. Wu, F. Dörfler, M. R. Jovanović, Input-output analysis and decentralized optimal control of inter-area oscillations in power systems, IEEE Trans. Pow. Sys. 31 (3) (2016) 2434–2444.
- [15] S. Schuler, U. Münz, F. Allgöwer, Decentralized state feedback control for interconnected systems with application to power systems, Journal of Process Control 24 (2) (2014) 379–388.
- [16] B. Marinescu, B. Malle, H. Bourles, L. Rouco, Robust coordinated tuning of parameters of standard power system stabilizers for local and global grid objectives, in: PowerTech, Bucharest, IEEE, 2009.
- [17] L. Rouco, Coordinated design of multiple controllers for damping power system oscillations, International Journal of Electrical Power & Energy Systems 23 (7) (2001) 517–530.
- [18] T. Borsche, T. Liu, D. J. Hill, Effects of rotational inertia on power system damping and frequency transients, 54th Annual Conference on Decision and Control (CDC) (2015) 5940–5946.
- [19] K. Liao, Z. He, Y. Xu, G. Chen, Z. Dong, K. Wong, A sliding mode based damping control of DFIG for interarea power oscillations, IEEE Trans. Sustainable Energy 8 (1) (2017) 258 – 267.
- [20] A. Yaghoobi, M. Buygi, M. Shanechi, Designing coordinated power system stabilizers: A reference model based controller design, IEEE Trans. Power Systems 31 (4) (2016) 2914 – 2924.
- [21] Y. Liu, Q. H. Wu, X. X. Zhou, Coordinated switching controllers for transient stability of multi-machine power systems, IEEE Trans. Power Systems 31 (5) (2016) 3937 – 3949.
- [22] J. Taranto, A. do Bomfim, D. Falcao, N. Martins, Automated design of multiple damping controllers using genetic algorithms, Proc. IEEE Power Engineering Society. Winter Meeting (1999) 539 – 544.
- [23] A. Fuchs, M. Imhof, T. Demiray, M. Morari, Stabilization of large power systems using VSC-HVDC and model predictive control, IEEE Trans. Power Delivery 29 (1) (2014) 480 – 488.

- [24] X. Lei, E. Lerch, D. Povh, Optimization and coordination of damping controls for improving system dynamic performance, *IEEE Trans. Power Systems* 16 (3) (2001) 473–480.
- [25] Z. A. Obaid, L. Cipcigan, M. T. Muhssin, Power system oscillations and control: Classifications and PSSs’ design methods: A review, *Renewable and Sustainable Energy Reviews* 79 (2017) 839–849.
- [26] B. Marinescu, Residue phase optimization for power oscillations damping control revisited, *Electric Power Systems Research* 168 (2019) 200–209.
- [27] C. Kammer, A. Karimi, Decentralized and distributed transient control for microgrids, *IEEE Trans. Cont. Syst. Tech.* (99) (2017) 1–12.
- [28] J. C. Doyle, K. Glover, P. P. Khargonekar, B. A. Francis, State-space solutions to standard \mathcal{H}_2 and \mathcal{H}_∞ control problems, *IEEE Trans. Automatic control* 34 (8) (1989) 831–847.
- [29] P. Gahinet, P. Apkarian, A linear matrix inequality approach to \mathcal{H}_∞ control, *International journal of robust and nonlinear control* 4 (4) (1994) 421–448.
- [30] C. W. Scherer, Structured \mathcal{H}_∞ optimal control for nested interconnections: A state-space solution, *Systems & Control Letters* (2013) 1105–1113.
- [31] P. Apkarian, D. Noll, Structured \mathcal{H}_∞ -control of infinite-dimensional systems, *International Journal of Robust and Nonlinear Control* 28 (9) (2018) 3212–3238.
- [32] A. Hassibi, J. How, S. Boyd, A path-following method for solving BMI problems in control, in: *American Control Conference (ACC)*, Vol. 2, IEEE, 1999, pp. 1385–1389.
- [33] S. Ibaraki, M. Tomizuka, Rank minimization approach for solving BMI problems with random search, in: *American Control Conference (ACC)*, Vol. 3, IEEE, 2001, pp. 1870–1875.
- [34] Q. Dinh, S. Gumussoy, W. Michiels, M. Diehl, Combining convex-concave decompositions and linearization approaches for solving BMIs, with application to static output feedback, *IEEE Trans. Automatic Control* 57 (6) (2012) 1377–1390.
- [35] J. Han, R. Skelton, An LMI optimization approach for structured linear controllers, *42nd IEEE International Conference on Decision and Control* (5) (2004) 5143 – 5148.
- [36] A. Karimi, H. Khatibi, R. Longchamp, Robust control of polytopic systems by convex optimization, *Automatica* 43 (8) (2007) 1395–1402.
- [37] S. Schuler, M. Gruhler, U. Münz, F. Allgöwer, Design of structured static output feedback controllers, *IFAC Proceedings Volumes* 44 (1) (2011) 271–276.
- [38] G. Befekadu, I. Erlich, Robust decentralized controller design for power systems using matrix inequalities approaches, in: *Power Eng. Soc. General Meet.*, IEEE, 2006.
- [39] A. Mešanović, D. Unsel, U. Münz, C. Ebenbauer, R. Findeisen, Parameter tuning and optimal design of decentralized structured controllers for power oscillation damping in electrical networks, in: *Proc. Amer. Cont. Conf. (ACC)*, IEEE, 2018, pp. 3828–3833.
- [40] S. Gumussoy, D. Henrion, M. Millstone, M. L. Overton, Multiobjective robust control with HIFOO 2.0, *Proc. 6th IFAC Symposium on Robust Control Design* 42 (6) (2009) 144–149.
- [41] P. Apkarian, D. Noll, Nonsmooth H-infinity synthesis, *IEEE Trans. Automatic Control* 51 (1) (2006) 71 – 86.
- [42] S. Kanev, C. Scherer, M. Verhaegen, B. De Schutter, Robust output-feedback controller design via local BMI optimization, *Automatica* 40 (7) (2004) 1115–1127.
- [43] S. Boyd, M. Hast, K. Åström, MIMO PID tuning via iterated LMI restriction, *International Journal of Robust and Nonlinear Control* 26 (8) (2016) 1718–1731.
- [44] A. Mešanović, U. Münz, R. Findeisen, Coordinated tuning of synchronous generator controllers for power oscillation damping, in: *Innovative Smart Grid Technologies Conference Europe*, IEEE, 2017.
- [45] A. Mešanović, U. Münz, R. Findeisen, Coordinated tuning of controller parameters in AC/DC grids for power oscillation damping, in: *IEEE/PES Transmission and Distribution Conference and Exposition*, 2018.
- [46] J. Lunze, *Regelungstechnik 2: Mehrgrößensysteme Digitale Regelung*, Springer-Verlag, 2013.
- [47] B. Poola, D. Gross, F. Dörfler, Placement and implementation of grid-forming and grid-following virtual inertia and fast frequency response, *IEEE Trans. Pow. Sys.* (2019).
- [48] S. Püschel-Løvengreen, P. Mancarella, Frequency response constrained economic dispatch with consideration of generation contingency size, in: *Power Systems Computation Conference (PSCC)*, IEEE, 2018.
- [49] J. Schiffer, D. Zonetti, R. Ortega, A. M. Stanković, T. Sezi, J. Raisch, A survey on modeling of microgrids-from fundamental physics to phasors and voltage sources, *Automatica* 74 (2016) 135–150.
- [50] MathWorks, Excitation system, <https://de.mathworks.com/help/physmod/sps/powersys/ref/excitationsystem.html> (Jan 2020).
- [51] A. Moeini, I. Kamwa, P. Brunelle, G. Sybille, Open data IEEE test systems implemented in simpowersystems for education and research in power grid dynamics and control, in: *Power Engineering Conference (UPEC)*, 2015 50th International Universities, IEEE, 2015, pp. 1–6.
- [52] MathWorks, Steam turbine and governor, <https://www.mathworks.com/help/physmod/sps/powersys/ref/steamturbineandgovernor.html> (Jan 2020).
- [53] IEEE, IEEE recommended practice for excitation system models for power system stability studies, *IEEE Std 421.5-2005 (Revision of IEEE Std 421.5-1992)* (2006) 1–93doi:10.1109/TEESTD.2006.99499.
- [54] A. Rahmoun, A. Armstorfer, H. Biechi, A. Rosin, Mathematical modeling of a battery energy storage system in grid forming mode, in: *Power and Electrical Engineering of Riga Technical University (RTUCON)*, 58th Intl. Sci. Conf. on, IEEE, 2017, pp. 1–6.
- [55] Sinamics inverter, <https://www.siemens.com/global/en/home/products/drives/sinamics.html> (Jan 2020).
- [56] S. Boyd, C. Desoer, Subharmonic functions and performance bounds on linear time-invariant feedback systems, *IMA Journal of Mathematical control and Information* 2 (2) (1985) 153–170.
- [57] S. Boyd, C. Barratt, *Linear controller design: limits of performance*, Tech. rep., Stanford University Stanford United States (1991).
- [58] K. Zhou, J. Doyle, *Essentials of robust control*, Prentice hall Upper Saddle River, NJ, 1998.
- [59] D. Uherka, A. Sergott, On the continuous dependence of the roots of a polynomial on its coefficients, *The American mathematical monthly* 84 (5) (1977) 368–370.
- [60] B. De Moor, S. Boyd, Analytic properties of singular values and vectors, *KTH Leuven, Belgium Tech. Rep* 28 (1989) 1989.
- [61] J. Nocedal, S. Wright, *Numerical optimization*, Springer, 2006.
- [62] J. Lofberg, YALMIP : a toolbox for modeling and optimization in MATLAB, *IEEE Int. Conf. on Robotics and Automation* (2004) 284 – 289.
- [63] J. F. Sturm, Using SeDuMi 1.05, a Matlab toolbox for optimization over symmetric cones (Jan 2020). URL https://sedumi.ie.lehigh.edu/?page_id=58
- [64] Mathworks, Sandscape power systems, <https://www.mathworks.com/products/simpower.html> (Jan 2020).
- [65] A. Mešanović, U. Münz, J. Bamberger, R. Findeisen, Controller tuning for the improvement of dynamic security in power systems, in: *IEEE PES Innovative Smart Grid Technologies Conf. Europe*, IEEE, 2018.
- [66] DynaGridCenter, Dynagridcenter, <http://forschung-stromnetze.info/projekte/dynamische-stromnetze-sicher-beherrschen/> (Jan 2020).
- [67] IREN2 - future oriented electricity grids for integration of renewable energy systems, <http://www.iren2.de/en/> (Jan 2020).
- [68] D. Groß, M. Colombino, J. Brouillon, F. Dörfler, The effect of transmission-line dynamics on grid-forming dispatchable virtual oscillator control, *IEEE Trans. Cont. of Network Syst.* (2019).
- [69] J. Chen, T. O’Donnell, Parameter constraints for virtual synchronous generator considering stability, *IEEE Trans. Power Syst.* 34 (3) (2019) 2479–2481.
- [70] A. Mešanović, X. Wu, S. Schuler, U. Münz, F. Dörfler, R. Findeisen, Optimal design of distributed controllers for large-scale cyber-physical systems, in: *Design Automation of Cyber-Physical Systems*, Springer, 2019, pp. 181–210.
- [71] Mathworks, systune, <https://www.mathworks.com/help/control/ref/systune.html> (Jan 2020).

Appendix A. Application of Theorem 3

To underline the claim of Theorem 3, we consider the small system

$$G'(s) = \begin{pmatrix} \frac{s+2}{(s+1)(s+3)} & \frac{s-3}{s^2+3s+3} \\ \frac{s^2+4s+10}{(s+3)(s^2+s+1)} & \frac{s+4}{(s+1)(s+2)} \end{pmatrix} \quad (\text{A.1})$$

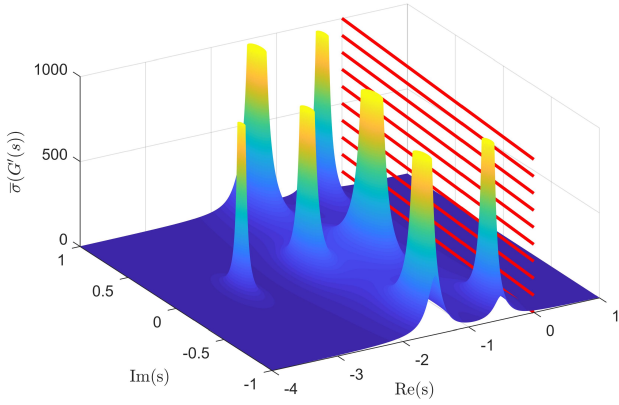


Figure A.29: Graphical representation of $\bar{\sigma}(G'(s))$; $\bar{\sigma}(G'(s))$ approaches infinity in the surrounding of any $s_{pij} \in \tilde{\mathcal{S}}$. Red lines mark where the system \mathcal{H}_∞ norm is minimized.

Table A.10: The initial step size $\Delta \mathbf{K}$ for the controller parameters of each power plant in the IEEE 39 bus system, shown in Figs. 3- 5.

	$R_{p,i}$	$K_{A,i}$	$T_{fd,i}$	$K_{fd,i}$	$K_{S,i}$	$T_{w,i}$	$T_{1,i}$	$T_{2,i}$	$T_{3,i}$	$T_{4,i}$
$\Delta \mathbf{K}$	0.05	60	500	1	6	50	1	50	1	50

This system has the pole set $\tilde{\mathcal{S}} = \{-1, -2, -3, -1.5 \pm j0.87, -0.5 \pm j0.87\}$, where the poles $s = -1$, and $s = -2$ have a multiplicity of 2. Figure A.29 shows the largest singular value of $G'(s)$. It confirms that the system singular values approach infinity as s approaches one of the system poles, see Lemma 2. We minimize the \mathcal{H}_∞ norm of the system by minimizing the largest singular value of G' on the imaginary axis, i.e. $\bar{\sigma}(G'(j\omega))$. The plane with $\text{Re}(s) = 0$, along which $\bar{\sigma}(G'(j\omega))$ is minimized, is represented with red lines in Fig. A.29. If the poles approach the imaginary axis, $\max_{\omega \in \mathbb{R}} \|\bar{\sigma}(G'(j\omega))\|_\infty$ rises to large values. Since the \mathcal{H}_∞ norm is minimized in every optimization step, the minimization of the \mathcal{H}_∞ norm will never lead to the system poles reaching, and crossing, the imaginary axis.

Appendix B. Controller models used for the IEEE 39 bus 10 power plant model

Figures 3, 4, and 5 show the power plant controller models used for modeling of the IEEE 39 bus grid in Subsection 4.1. All models are a part of the system proposed in [51]. We optimize the gain $K_{A,i}$ of the AVR_{*i*}, shown red in Fig. 3. We also optimize all parameters of PSS_{*i*}, except the physically-determined sensor time constant, marked red in Fig. 4. The governor and turbine model, shown in Fig. 5, has one optimization parameter, marked in red. It is the proportional gain of the governor. All presented models are standard IEEE models. The initial maximal allowed step size for all controllers is shown in Table A.10.

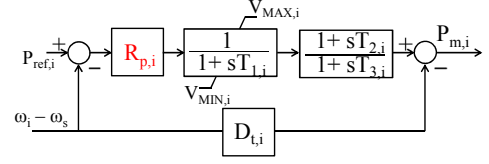


Figure B.30: The TGOV1 turbine and governor model used for the power system model in Subsection 4.2. The frequency droop gain of the governor $R_{p,i}$ is an optimization variable.

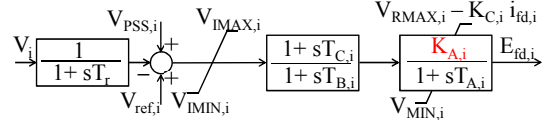


Figure B.31: The standard EXAC4 model of the AVR_{*i*}, where $T_{r,i}$ is the transducer time constant, $T_{C,i}$ and $T_{B,i}$ are dynamic gain reduction time constants, $K_{A,i}$ is the AVR gain, and $T_{A,i}$ is the AVR lag time constant. We assume that $K_{A,i}$, marked red, is tunable.

Appendix C. Controller models used for the 53 generator power system model

The reduced European grid defined in Subsection 4.2 uses controllers shown in Figs. B.30, B.31, and B.32. Similar to the IEEE 39 bus controller models, the gains of TGOV_{*i*} and AVR_{*i*} are tuned, as well as all parameters of PSS_{*i*}. For this power system, the standard model TGOV1 is used for TGOV_{*i*}, the EXAC4 model is used for AVR_{*i*}, and the IEEE PSS 1A model is used for PSS_{*i*}. All presented controller models are standard IEEE models.

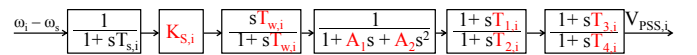


Figure B.32: The standard IEEE PSS 1A model, where $K_{S,i}$ is the PSS gain, $T_{w,i}$ is the washout time constant, $T_{1,i}$ - $T_{4,i}$ are the lead-lag filters time constants, $T_{s,i}$ is the sensor time constant, and A_1 and A_2 are notch filter parameters. All of the PSS parameters are tunable, except the sensor time constant.